Identification of early neurodegenerative pathways in progressive multiple sclerosis

Kaufmann M., Schaupp A.L., Sun R., Coscia F., Dendrou C.A., Cortes A., Kaur G., Evans H.G., Mollbrink A., Navarro J.F., Sonner J.K., Mayer C., DeLuca G.C., Lundeberg J., Matthews P.M., Attfield K.E., Friese M.A., Mann M., Fugger L.

This is the final version of the accepted manuscript. The original article has been published in final edited form in:

Nature Neuroscience
2022 JUL ; 25(7): 944–955
2022 JUN 20 (first published online: final version)
doi: 10.1038/s41593-022-01097-3

URL: https://www.nature.com/articles/s41593-022-01097-3

Publisher: Nature Research (Springer Nature)

Identification of early neurodegenerative pathways in progressive multiple sclerosis

Max Kaufmann[1,2,14], Anna-Lena Schaupp[2,14], Rosa Sun[2,3,4], Fabian Coscia[3,5], Calliope A. Dendrou[2,6], Adrian Cortes[2], Gurman Kaur[2,7,8], Hayley G. Evans[2], Annelie Mollbrink[9], José Fernández Navarro[9], Jana K. Sonner[1], Christina Mayer[1], Gabriele C. DeLuca[10], Joakim Lundeberg[9], Paul M. Matthews[11,12], Kathrine E. Attfield[2], Manuel A. Friese[1], Matthias Mann[3,13], Lars Fugger[2,7,15,*]

[1] Institut für Neuroimmunologie und Multiple Sklerose, Zentrum für Molekulare Neurobiologie Hamburg, Universitätsklinikum Hamburg-Eppendorf, Hamburg, Germany

[2] Oxford Centre for Neuroinflammation, Nuffield Department of Clinical Neurosciences, John Radcliffe Hospital, University of Oxford, Oxford, UK

[3] Proteomics Program, Novo Nordisk Foundation Center for Protein Research, University of Copenhagen, Copenhagen, Denmark

[4] Department of Neurosurgery, Queen Elizabeth Hospital, B15 2TH Birmingham, UK

[5] Spatial Proteomics Group, Max Delbrück Center for Molecular Medicine in the Helmholtz Association, Berlin, Germany

[6] Nuffield Department of Medicine, Wellcome Centre for Human Genetics, University of Oxford, Oxford, UK

[7] MRC Human Immunology Unit, Weatherall Institute of Molecular Medicine, John Radcliffe Hospital, University of Oxford, Oxford, UK

[8] Klarman Cell Observatory, Broad Institute of MIT and Harvard, Cambridge, MA, USA

[9] Department of Gene Technology, KTH Royal Institute of Technology, Science for Life Laboratory, Solna, Sweden

[10] Nuffield Department of Clinical Neurosciences, John Radcliffe Hospital, Oxford, UK

[11] Department of Brain Sciences, Imperial College London, London, UK

[12] UK Dementia Research Institute, Imperial College London, London, UK

[13] Department of Proteomics and Signal Transduction, Max Planck Institute of Biochemistry, Martinsried, Germany

[14] These authors contributed equally

[15] Lead contact

* Correspondence: lars.fugger@imm.ox.ac.uk

Abstract

Progressive multiple sclerosis (MS) is characterized by unrelenting neurodegeneration, which causes cumulative disability and is refractory to current treatments. Drug development to prevent disease progression is an urgent clinical need yet is constrained by an incomplete understanding of its complex pathogenesis. Using spatial transcriptomics and proteomics on fresh-frozen human MS brain tissue, we identified multicellular mechanisms of progressive MS pathogenesis and traced their origin in relation to spatially distributed stages of neurodegeneration. By resolving ligand–receptor interactions in local microenvironments we discovered defunct trophic and anti-inflammatory intercellular communications within areas of early neuronal decline. Proteins associated with neuronal damage in patient samples showed mechanistic concordance with published *in vivo* knockdown and CNS disease models, supporting their causal role and value as potential therapeutic targets for progressive MS. Our findings provide a new framework for drug development strategies, rooted in an understanding of the complex cellular and signaling dynamics in human diseased tissue, that facilitate this debilitating disease.

Main text

Introduction

Multiple sclerosis (MS) is a common and disabling autoimmune disease of the central nervous system (CNS), presenting in most patients with a relapsing-remitting course followed by an overt progressive disease phase[1]. Current disease modifying therapies are highly effective in preventing symptomatic relapses[2], which are characterized by white matter lesions caused by inflammatory CNS-infiltrating immune cells. In contrast, progressive disease, where gray matter atrophy and neurodegeneration predominate[3–6], is unresponsive to treatment beyond suppressing a residual relapsing-remitting disease component[7–9].

Developing new treatment options for progression could greatly benefit from systematically measuring and understanding underlying molecular pathways of neurodegeneration *in situ* in human post-mortem brain tissue from MS patients[10]. Here we applied spatial transcriptomics[11] with high sensitivity proteomics[12,13] and integrated our data with published scRNA-seq and *in vivo* perturbation model data to (i) systematically dissect underlying disease components of progressive MS with high granularity in the context of spatially resolved neurodegeneration, (ii) identify ligand-receptor interactions associated with these components and (iii) prioritize CNS-enriched receptors as new drug targets that can address the complex pathogenesis of progressive MS.

Results

Spatial transcriptomics tracks neurodegeneration

To systematically delineate neurodegenerative pathways across cortical gray matter regions with intact neurons towards regions characterized by neuronal decline, we performed spatial

transcriptomics on fresh-frozen post-mortem cortical brain tissue from 13 progressive MS patients and 5 controls (Fig. 1a) (Supplementary Table 1). Given the low treatment prevalence in this cohort (Supplementary Table 1) and that none of the applied therapies have shown a clinically significant effect on progressive MS in large phase III studies[7], or to the patients analyzed here, a potential drug bias on our results is unlikely. The tested cohort was comprised of patients with a long average disease duration of 22.6 years, who had converted from a relapsing-remitting to a secondary progressive disease course on average 11.6 years before the time of death and of which 11 out of 13 patients persistently required a wheelchair before they died (Supplementary Table 1). Thus, in line with common clinical experience and the current literature, the patient collective studied here is expected to be largely representative of a phase of MS, where continuous neurodegeneration-associated disease progression predominates over relapse associated blood-brain-barrier breaches[1]. A total of 37 tissue sections were analyzed (32 MS sections and 5 control sections), all of which included cortical gray matter tissue, except for one control section that only consisted of white matter. Up to 6 regions (6.5 mm x 6.9 mm) per section were sampled with 1,007 spatially barcoded mRNA-capturing spots. Hematoxylin / eosin (HE) stained microscopy images were available for all sections and were assessed by neuropathologists for structural features; accordingly, the images and spot transcriptomes were annotated on a pixel-wise basis, allowing the computational isolation of gray matter areas from contamination by white matter, sulcus areas or meninges (Fig. 1a). After filtering for gray matter spots transcriptomes in this manner, 174 of 210 sampling areas were used for a focused analysis of neurodegeneration. In gray matter spot transcriptomes, a mean of 4,328 unique molecular identifiers (UMIs) were recovered and 2,191 genes were detected.

To track neurodegeneration in the gray matter, we first mapped an intact neuronal signature to all spot transcriptomes, which was extracted in contrast to non-neuronal cell types from publicly available single nuclei RNA-sequencing (snRNA-seq) datasets of healthy cortical brain tissue (Extended Data Fig. 1, Supplementary Table 2)[14–17]. Comparison of MS patients

with control cases revealed a striking reduction of the intact neuronal signature in MS patients, identifying a shift towards an MS-associated neurodegenerative state (Fig. 1b). This was further corroborated by neuropathologic assessment of adjacent tissue sections that identified lesions corresponding to our transcriptomic readout (Extended Data Fig. 2). Strikingly, utilizing spatial transcriptomics data in this manner was able to provide an enhanced resolution of the heterogenous distribution of neurodegeneration within the tissue and across patients (Fig. 1c,d). Thus, when combining all sampling areas, a pseudo-temporal pattern of neurodegeneration could be defined, allowing us to infer early events in neurodegeneration when therapeutic intervention could prove most beneficial. Specifically, we could identify gray matter (GM) areas in MS patient brains, which showed an enrichment of the intact neuronal signature within the same range as control samples, which we classified as 'MS GM intact' (Fig. 1b). These intact areas were also defined in contrast to areas with a reduced intact neuronal signature compared to control tissue, classified as 'MS GM degenerating' (Fig. 1b), allowing the identification of upstream events that contribute to neurodegeneration.

MS neurodegenerative pathways act across cell types

To characterize the biological components of neurodegeneration in progressive MS, we first identified groups of genes (modules) whose expression was jointly altered across different stages of neuronal decline represented in distinct sampling regions (Fig. 2a,b). Each module was annotated functionally, as defined by gene ontology (GO) term enrichment analyses (Fig. 2b, Extended Data Fig. 3, Supplementary Table 3). Biological processes represented within these modules included synapse assembly, synaptic communication and plasticity, regulation of neuronal projections, myelination, immune cell activation and tissue remodeling. Subsequent integration with single cell data[14–18] showed that the genes identified in each module were predominantly expressed by only one cell type. However, numerous edges bridging across modules in the co-expression graph revealed that their regulation was highly connected between cell types, implying a strong co-dependency of pathogenic processes in

progressive MS that is mediated by intercellular communication (Fig. 2b,c). To then prioritize the most relevant modules associated with the progression of neurodegeneration, and to determine the directionality of their regulation, we correlated the summarized expression (eigengene) values of each module with the reduction of the intact neuronal signature in the same gray matter locations (Fig. 2d–g). Modules relating to synaptic communication, synaptic plasticity and maintenance of neuronal projections showed progressively diminishing expression with greater neurodegeneration (Fig. 2d). In contrast, processes relating to inflammation and tissue remodeling that mapped to innate immune cells and astrocytes were increasingly upregulated (Fig. 2f). Interestingly, oligodendrocyte-driven myelination was also upregulated with reduction of the intact neuronal signature, indicating that neurodegeneration occurs in progressive MS despite active myelination pathways (Fig. 2f). Notably, inflammatory pathways were minimally expressed in areas with normal expression of the intact neuronal signature (Fig. 2f). However, downregulation of pathways relating to synapses and axons was already observed in intact MS gray matter, implying that these changes are triggered early during neurodegeneration and are not explained by the influence of inflammation alone (Fig. 2d).

To confirm our results at the protein level, we applied high sensitivity mass spectrometry to spatially defined samples (<0.06 mm^3) of adjacent tissue regions[12,13]. A total of 4,541 unique proteins were identified in 65 gray matter samples from 14 progressive MS patients (56 samples) and 7 controls (9 samples) (Fig. 3a,b, Supplementary Table 1). Enrichment of the previously defined intact neuronal signature was then tested across the tissue. Again, we observed a comparable pseudo-temporal continuum of reduced intact neuronal signature, as seen in the transcriptomic data (Fig. 3c). We then assessed the 4,093 genes with matching protein data to test for multimodal concordance of relationships between co-expression modules and neurodegeneration, as previously generated using all 12,674 genes (Fig. 3b,d). Directional agreement of modules in relation to neurodegeneration between the RNA and protein level was observed for all modules, with the exception of module 4 (‘neuron

projections') and module 8 ('Axo-dendritic protein transport'), which did not correlate with neurodegeneration on the protein level. These were subsequently excluded from further downstream analysis (Fig. 3d).

Early intercellular communication in MS neurodegeneration

Spatial transcriptomics provides a powerful discovery tool to identify ligand–receptor interactions governing disease components directly in the tissue[10]. Accordingly, to relate multimodally validated disease pathways to intercellular communication, we sought to identify ligand–receptor interactions that were altered with neurodegeneration. We assessed the expression of 1,396 curated ligand–receptor pairs[19] in 83,256 gray matter niches, deriving combined expression values where both partners were expressed within < 200 µm of one another (Fig. 4a, methods); a threshold which was based on established operating ranges of juxtacrine and paracrine signals[10]. This analysis yielded spatially resolved expression data for 428 ligand–receptor interactions, which, when further correlated with enrichment of the intact neuronal signature, allowed us to relate intercellular communication to a pseudo-temporal continuum of neurodegeneration (Fig. 4a).

Within this data set, we intentionally focused on the contrast between MS gray matter areas with preserved intact neuronal signature ('intact MS gray matter') compared to non-MS control tissue ('control gray matter') to identify ligand–receptor interactions important in the earliest stages in the pathogenic evolution of neurodegeneration, where therapeutic intervention is likely most feasible (Fig. 4b–l). In total, this approach yielded 61 ligand–receptor pairs: of these, 15 were decreased in intact MS gray matter and were further reduced in degenerating MS gray matter, and 46 were increased in intact MS gray matter, of which 16 were also increased in degenerating MS gray matter, while 30 were reduced to or below control levels (Fig. 4d). To test for a potential age- or sex-based bias in our results, owing to an imbalance between the MS patient samples and the controls (Supplementary Table 1), we systematically

explored which genes in the human genome show age- or sex-dependent expression changes in the human cortex in *n* = 336 donors from the GTEx consortium (Extended Data Fig. 4a–c, methods). No systematic age- or sex-bias was observed in the set of differentially co-expressed ligand/receptor genes and thus these were not considered to be potential confounders in our results.

Then, as a validation of our approach, we calculated log2 fold changes of ligand and receptor gene expression in intact MS gray matter compared to control gray matter both for spatial transcriptomics and high sensitivity proteomics data. Ligands and receptors detected at the RNA and protein level showed significant positive correlation between the modalities (r = 0.41, FDR-adjusted *p* value = 0.044, Extended Data Fig. 4d). Furthermore, several of the identified ligand–receptor pairs, including *CXCL12-CXCR4*, *CCL5-CCR1*, *POMC-MC1R*, *CD47-SIRPA* and *IL6-IL6R/IL6ST* have well established roles in MS pathology[20–25] (Fig. 4d). However, the majority of our findings have not previously been described for progressive MS and thus reveal a wealth of novel, mechanistic and potentially therapeutic insights into this disease.

To identify mechanistic patterns in the intercellular communication of early stages of MS neurodegeneration, we annotated each ligand–receptor pair with previously published biological functions (Supplementary Table 4). The most pronounced themes were anti-inflammatory interactions (25% of all candidate interactions, defined as immunosuppressive), pro-inflammatory interactions (25%, defined as facilitating immune responses) and trophic interactions (31%, defined as growth factors contributing to development, proliferation or cell survival) (Fig. 4d).

Competing pro- and anti-inflammatory communications were present in intact MS gray matter and appeared to both have multiple layers of redundancy (Fig. 4d–h). For example, the potent innate immunity suppressors *GAS6–TYRO3* and *CD47–SIRPA*[26,27] were downregulated in intact MS gray matter and further repressed in degenerating gray matter (Fig. 4d–h). In their

place, other anti-inflammatory interactions surged in intact MS gray matter, some of which were further upregulated in degenerating areas, such as *HLA-F–LILRB1* and *BST2–LILRA4*[28,29], while the majority were reduced in degenerating areas, as exemplified by *CX3CL1–CX3CR1*, *POMC–MC1R* and *PROS1–AXL*[21,30,31] (Fig. 4d,h). In parallel, we also observed pro-inflammatory interactions, including *C3–C3AR1*, *CCL5–CCR1* and *ALOX5–ALOX5AP*, arising in the intact MS gray matter that largely remained present or increased further in degenerating cortical gray matter areas[25,32,33] (Figure 4d–h). The balance of pro- and anti-inflammatory stimuli in intact MS gray matter matched the overall low expression of inflammation-associated gene modules we observed early during neurodegeneration (Fig. 2f) and revealed receptors that could be therapeutically targeted to potentially preserve or induce such a state.

A second, striking theme that we observed was how trophic interactions, which support cell viability and growth, were reduced in intact MS gray matter compared to non-MS control tissue, with further reductions seen in degenerating areas. Interacting partners included members of the growth factor families TGF, FGF and VEGF *and PSAP–GPR37L1*[34] (Fig. 4d,i–l , Supplementary Table 4). Compensatory trophic interactions were upregulated in their place in intact MS gray matter, but were also reduced in degenerating areas (Fig. 4d,i–l, Supplementary Table 4). These findings suggest that the growth factor environment in the gray matter of progressive MS patients is altered, even in the absence of overt neurodegeneration and is fully suppressed in its presence.

To contextualize these findings, we next sought to map them to specific cell types. For this purpose, we integrated our spatial transcriptomics data with snRNA-seq data of cortical gray matter[14–17] and scRNA-seq data of blood immune cells[18] using enrichment score-based deconvolution[10]. We validated the robustness of this approach by comparing these findings against three alternative integration methods: RCTD[35], spatialDWLS[36] and SPOTlight[37]. Each method generated significantly correlated results, both in comparison with each other, as well

as with our primary enrichment score-based deconvolution method (Extended Data Fig. 5). Based on the cell type deconvolution the contribution of CNS-resident and -invading cell types to ligand–receptor interactions could then be modeled (Fig. 5a–i). Notably, due to method-inherent constraints, this approach cannot distinguish between differential gene expression and differential cell type composition of spot transcriptomes, in all cases. For example, a pro-inflammatory interaction may either occur because microglial cells have upregulated a pro-inflammatory ligand, or because microglia expressing this ligand move into this location. In either scenario, a pathogenic mechanism is identified and thus has potential therapeutic value.

Interactions reduced in intact MS gray matter compared to controls ('Up in contr. GM') typically occurred between neurons, oligodendrocytes and astrocytes (Fig. 5d,g). These interactions frequently included trophic interactions and some guidance cues for myelination and neuronal projections. Interestingly, multicellular trophic interactions revealed that oligodendrocytes, astrocytes and endothelial cells expressed the receptors, with neurons providing the ligands. For example, neuronal expression of *FGF9* and *NECTIN1*, as ligands for *FGFR3* on astrocytes and neuronal expression of *PSAP*, as ligand for *GPR37L1* on oligodendrocytes (Fig. 5d,g). Conversely, growth factor receptors on neurons were predicted to be stimulated by interactions among neurons, as exemplified by neuronal *VEGFA* production and neuronal expression of the VEGF receptors *NRP1* and *NRP2* (Fig. 5d,g). These findings highlight neurons as important sources of survival signals in the CNS and suggest that neurodegeneration may precipitate the degeneration of other cell types.

Interactions most abundant in intact MS gray matter ('Up in MS GM intact') were characterized by a remarkable increase in cell type diversity involving multifaceted communication between neurons, oligodendrocytes, oligodendrocyte precursor cells (OPC), endothelial cells, astrocytes, microglia and monocytes (Fig. 5e,h). In this network, neurons received trophic input from *GDF11*-expressing oligodendrocytes and provided alternative growth factors to the tissue such as *MET* to *HGF*-expressing astrocytes, *WNT5A* to *FZD5*-expressing

oligodendrocytes and *PDGFB* and *PDGFC* to *PDGFRA*-expressing OPCs (Fig. 5e,h). Simultaneously, inflammation-associated interactions arose that involved microglia and endothelial cells in communication with the other cell types. For example, we observed oligodendrocytes providing microglia with *CSF1* driving their activation and survival[38], invading monocytes providing microglia with *TNFSF10*, known to increase cytokine production[39] and endothelial cells providing cues that undermine blood-brain barrier integrity (*ANGPT2–TEK*) and serve to attract invading immune cells from the blood (*CCL2-ACKR1*)[40,41] (Fig. 5e,h). This surge in pro-inflammatory communication was counterbalanced by anti-inflammatory signals from neurons including *PROS1*, *POMC* and *CX3CL1* and from astrocytes via *TGFB2*[42] (Fig. 5e,h).

Interactions further upregulated in degenerating MS gray matter ('Up in MS GM degen.') were dominated by microglia together with some contributions by endothelial cells and invading monocytes. Neuronal growth factor expression and control of inflammation was no longer apparent at this stage and only some anti-inflammatory cues were provided by astrocytes via *ANXA1* (Fig. 5f,i). Notably, while we now observed the presence of several chemotactic and activating stimuli for microglia including *ALOX5AP*, *C3*, *HEBP1*[43] and *CCL5*, the role of microglia in neurodegeneration is potentially heterogenous. For instance, microglia expressed *GRN* that limits inflammation by blocking TNF receptors on monocytes[44] and *BST2* that restrains microglial cytokine production by interaction with *LILRA4*.

When taken together, seemingly intact gray matter areas in progressive MS patients appear to exhibit competing protective and pathogenic features, where the outcome of cell survival may depend on specific anti-inflammatory and trophic cues in addition to inflammation itself.

Animal models validate a role of target genes in CNS-damage

To test whether our prioritization of ligand–receptor interactions associated with early neurodegeneration in progressive MS had successfully identified causal genes, which are suitable for therapeutic targeting, we employed two complementary strategies. Firstly, we tested the phenotypic effect of all candidate sets of ligand–receptor genes (pro-inflammatory candidates, anti-inflammatory candidates and trophic candidates) using published data from a genome-wide *in vivo* knock-down screen for essential CNS genes[45] (Fig. 6a). Secondly, we systematically assessed the effects of perturbations of our candidate genes using multiple published *in vivo* CNS disease models representing a broad spectrum of CNS-injury pathways (Fig. 6b, Supplementary Table 5).

Published *in vivo* knock-down data for our candidate ligand–receptor gene sets revealed significant depletion of CNS cells (phenotype strength) when compared to ligand–receptor gene sets of the same mean size, randomly selected from the input data (95%-confidence interval) (Fig. 6a,c). Furthermore, our candidate gene sets contained significantly more essential CNS genes (symptomatic knockdowns) overall (Fig. 6c), with the strongest protective effect observed for the set of trophic candidates (99%-confidence interval). Interestingly, the set of pro-inflammatory genes also contained several genes, which contributed to the survival of CNS cells, placing the eligibility of proinflammatory targets for therapeutic inhibition in progressive MS into question.

A systematic literature search for published experiments involving our candidate genes, as well as several classes of *in vivo* CNS disease models, resulted in 2,945 identified studies that included combinations of our search terms in the title and/or abstract (Fig. 6b, Supplementary Table 5). Manual annotation of all publications was performed to select only those experiments, where one of our candidate genes was specifically perturbed *in vivo* (i.e. knockout, overexpression, activating treatment, inhibiting treatment) and a clinically relevant

readout was reported (amelioration, exacerbation or no effect on the model) (Fig. 6b,d). The tested classes of disease models comprised a broad spectrum of etiologies, including primary neurodegeneration such as Alzheimer's disease (AD) and Parkinson's disease (PD), inflammation-mediated CNS-injury, such as in experimental autoimmune encephalitis (EAE, commonly used as a model for relapsing-remitting MS) and CNS hypoxia (stroke). In total, 308 perturbational experiments could be identified, which included matches for 58 out of 106 (55%) candidate ligand–receptor genes. This amounted to relevant perturbation data for at least one interaction partner for 46 out of 61 (75%) ligand–receptor pairs that were differentially co-expressed between intact MS gray matter and control samples (Supplementary Table 5). Underscoring the causal nature of our candidate genes, the majority of assessed genes showed a net positive or net negative effect on *in vivo* CNS disease models, with only 6 genes showing no conclusive effect (Fig. 6d). However, we note that a reporting bias may artificially reduce this number. Pro-inflammatory candidates were mostly detrimental to CNS disease models, whereas anti-inflammatory and trophic candidates largely played protective roles (Fig. 6d). Notably, pro-inflammatory and anti-inflammatory candidate genes often had ambiguous effects between different disease models and sometimes within one disease model. For example, the majority of published experiments suggested a detrimental role for *CSF1R* in CNS disease models, but this effect was predominantly driven by AD models and EAE, whereas stroke models could go either way and ALS models were positively affected (Fig. 6d). Echoing the results from the genome-wide knockdown screen, this may suggest that targeting inflammation-associated molecules to amend neurodegeneration in progressive MS could have ambiguous effects. Conversely, most trophic candidate genes were unambiguously protective. A notable example where mechanistic ambiguity has been resolved through experimentation is the anti-inflammatory interaction between *CD47* and *SIRPA*. Here, published *in vivo* disease model data is almost exclusively in EAE, where these factors are required for the initiation of the disease, thus demonstrating a detrimental function (Fig. 6d). However, a more detailed dissection of this phenotype[20] has shown that *SIRPA*–*CD47* interactions provide a protective role when there is evidence of CNS injury in established

disease, which parallels other lines of evidence suggesting both an anti-inflammatory and neuroprotective role[26,46,47].

Prioritizing new therapeutic targets for MS neurodegeneration

To investigate the relationship between ligand–receptor interactions and underlying processes of neurodegeneration, we correlated the occurrence of each ligand–receptor interaction to the regulation of gene co-expression modules in the same gray matter locations (Fig. 7a). We observed that most modules strongly correlated with the presence of at least one candidate ligand–receptor interaction that was up- or downregulated in intact MS gray matter (Extended Data Fig. 6). For example, module 1 ('synapse assembly') showed a strong relation with *CD47–SIRPA*, module 3 ('myelination') was strongly positively correlated with *FGF1–FGFR3* and module 7 ('myeloid cell differentiation') was positively associated with homophilic interaction of *ESAM* (Extended Data Fig. 6). Moreover, a subset of interactions exhibited broad connectivity with several modules. For example, *PSAP–GPR37L1* was among the most strongly correlated interactions for module 1 ('synapse assembly'), module 2 ('neurotransmitter secretion'), module 3 ('myelination'), and module 7 ('myeloid cell differentiation') (Extended Data Fig. 6). To formalize and stratify the breadth of the relations between candidate interactions and modules we derived the mean absolute correlation of each candidate ligand–receptor interaction with all modules (Fig. 7a,b, Supplementary Table 4). The scores of interactions ranged from 0.14 to 0.45, topped by *PSAP–GPR37L1* (0.45), *GAS6–TYRO3* (0.41), *CD47–SIRPA* (0.40), *CADM3–CADM4* (0.40) and *FGF1–FGFR3* (0.38) (Fig. 7b, Supplementary Table 4). The strong overall module correlation of these candidates was driven by positive association with CNS-related processes, such as synaptic communication and myelination as well as negative correlation with immune related processes (Fig. 7b, Extended Data Fig. 6). Taking the mean absolute module correlation for all interactions into account, we observed a significant separation of trophic and anti-inflammatory interactions from the group of pro-inflammatory interactions (Fig. 7b,c). The co-

expression of most pro-inflammatory interactions was narrowly linked to individual immune-related components of MS neurodegeneration and correlated poorly with CNS-related components (Fig. 7b). Conversely, the spatial co-expression of trophic and anti-inflammatory interactions was associated with modulation of a larger spectrum of pathogenic pathways, including immune-associated and CNS-related processes (Fig. 7b). These findings imply that chronic, inflammatory stress alone does not habitually lead to the full extent of multicomponent neurodegeneration in cortical brain tissue of MS patients, but that association with a local failure of trophic and anti-inflammatory intercellular communication appear to be required.

Notably, the prioritization of targets with broad effects in the CNS raises the possibility of undesired pleiotropic effects in other organs throughout the body potentially limiting the clinical applicability of such strategies due to side effects. To begin to address this concern, we analyzed the expression of our candidate receptors in a large post-mortem tissue data set from the Genotype-Tissue Expression (GTEx) project comprising 16,704 RNA-sequencing samples from 52 tissues of 948 donors[48]. For each receptor we compared mean expression in the brain cortex to mean expression in non-CNS tissues resulting in a CNS specificity score (Fig. 7d, Supplementary Table 4). With these, we determined the position of target receptors in a coordinate system defined between pleiotropic connection to multicomponent neurodegeneration (mean absolute module correlation) and enrichment in the CNS (CNS-specificity score) (Fig. 7d), where ideal therapeutic targets would maximize both traits. We observed several receptors that showed no enrichment for the CNS. For example, *PDGFRA*, whose spatial co-expression with *PDGFC* was broadly correlated with biological processes underlying neurodegeneration (mean absolute correlation coefficient 0.35), was expressed in a number of non-CNS tissues (CNS-specificity score 0.27), many of which showed a more pronounced expression, such as ovaries (Fig. 7e). Importantly, we found that several candidate interactions possessed both relatively broad correlation with processes underlying neurodegeneration (mean absolute correlation coefficient ≥ 0.35) as well as CNS-enriched receptor expression (CNS-specificity score > 1). These included *GPR37L1*, *TYRO3*, *SIRPA*,

CADM3 and *FGFR3* (Fig. 7d–h, Supplementary Table 4). Immunohistochemistry data from the human protein atlas[49] was available for several of our targets and validated their CNS-enriched expression on the protein level (Fig. 7i–l, Extended Data Fig. 7a,b). In addition to quantifying CNS specificity our approach also allowed us to qualify the observed expression patterns outside of the CNS. For instance, *CADM3* and *GPR37L1* showed relevant non-CNS expression only in the tibial nerve, where they are thought to carry out similar beneficial roles as in the CNS[50–52]. High non-CNS expression of *SIRPA* was only observed in the blood, where it is well known to limit innate immunity[26]. Agonistic targeting of *SIRPA* in MS would therefore be expected to have a desirable effect both on the CNS and on the peripheral immune system.

Discussion

Progressive MS is representative of a larger class of neurodegenerative diseases, including Alzheimer's disease, where a lack of knowledge about early events in neurodegeneration prohibits the identification of effective therapeutic approaches, leaving millions of patients without treatment options[53]. By applying spatial transcriptomics with high sensitivity proteomics directly in post-mortem human MS brain tissue, we tracked the changes of >4000 paired genes and proteins across spatially distributed stages of neurodegeneration. Crucially, ordering these micro-areas by increasing severity, in the manner of a pseudo-temporal trajectory of neuronal decline, exposed biological processes that are predicted to occur in early stages of neurodegeneration. These pathways were characterized by multiple levels of redundancy as well as high distribution across cell types. Further, we identified a local failure of trophic and anti-inflammatory cellular communication in early stages of neurodegeneration as well as demonstrating how pro-inflammatory factors can have ambiguous roles in disease pathogenesis. Together, these results would suggest that current drug targets fail to prove efficacious either through their restriction to specific cell types or due to their inability to impact those pathways identified here.

To validate potential novel drug targets for progressive MS from our findings, we assessed the mechanistic functions of the identified target candidates in a broad selection of *in vivo* CNS disease models, which supported their causal role in neurodegeneration. Furthermore, we incorporated the results of our detailed dissection of pathogenic components of progressive MS into the stratification of our target candidate list, prioritizing targets predicted to impact the maximal number of components of progressive MS pathogenesis at once. These targets included CNS-enriched receptors such as *GPR37L1*, *TYRO3*, *SIRPA* and *FGFR3*, some of which are already within drug development pipelines for human use [54–58].

To conclude, our study exemplifies the importance of understanding complex diseases directly within the affected tissue, permitting a wealth of new clinical insights and providing a unique biomedical source for new treatment modalities.

Acknowledgments

We thank Professor Margaret Esiri, University of Oxford, for advice and assistance in characterization of the post-mortem brain tissue and Professor Gil McVean, Big Data Institute, University of Oxford, for analytical support. MK is supported by a Clinician-Scientist Fellowship from the Stifterverband für die Deutsche Wissenschaft and a Walter- Benjamin-Fellowship of the Deutsche Forschungsgemeinschaft (KA5554/1-1, KA5554/1-2). FC is supported by the European Union's Horizon 2020 research and innovation program under grant agreement No 846795 (Marie Skłodowska-Curie Fellowship). PMM is supported by the Edmond J Safra Foundation and Lily Safra, an NIHR Senior Investigator Award and the UK Dementia Research Institute, which receives its funding from UK DRI Ltd., funded by the UK Medical Research Council, Alzheimer's Society and Alzheimer's Research UK. MAF is supported by intramural funds of the University Medical Center Hamburg-Eppendorf, the Deutsche Forschungsgemeinschaft (SFB1328, SPP1738, KFO296, FOR2289, FOR2879, FOR5068, FR1720/11-2), the Gemeinnützige Hertie-Stiftung, the Deutsche Multiple Sklerose Gesellschaft (DMSG; V6.2) and the Bundesministerium für Bildung und Forschung (Target validation, 16GW0308K). MM is supported by the Max Planck Society for the Advancement of Science and the Novo Nordisk Foundation (grant agreement NNF14CC0001 and NNF15CC0001), the European Union's Horizon 2020 research and innovation program under grant agreement 686547 (MSmed Project). LF is supported by the Wellcome (100308/Z/12/Z), the Medical Research Council UK (MC_UU_12010/3), the Oak Foundation (OCAY-15-520), and the NIHR Oxford BRC.

Author contributions

In order of appearance in the author list. **Conceptualization**, MK, ALS, KEA, MAF and LF; **methodology**, MK, ALS, RS, FC, CAD, AM, GCD and JL; **validation**, MK, FC and JFN; **formal analysis**, MK; **investigation**, MK, ALS, RS, FC, CAD, AC, GK, HGE, JFN, JKS, CM,

GCD and KEA; **resources**, AM, JL, PMM and MAF; **data curation**, MK; **writing - original draft**, MK, ALS, KEA, MAF and LF; **writing - review & editing**, MK, ALS, GCD, PMM, KEA, MAF and LF; **visualization**, MK; **supervision**, MAF, MM and LF; **funding acquisition**, MM and LF. We note that RS and FC (the third and fourth author) contributed equally.

Declaration of interests

GCD has received research funding from Merck-Serono, travel expenses from Bayer Schering, Biogen Idec, Genzyme, Merck Serono, Novartis and honoraria as an invited speaker/faculty/advisor for Novartis and Roche. JK and AM are scientific consultants for 10X Genomics. PMM has received consultancy fees from Roche, Adelphi Communications, Celgene, Neurodiem and Medscape, honoraria or speakers' fees from Novartis and Biogen and has received research or educational funds from Biogen, Novartis and GlaxoSmithKline. The remaining authors declare no competing interests.

Figure legends

Fig. 1: Spatial transcriptomics enables continuous tracking of neurodegeneration in progressive MS.

a, Summary of data collection. **b**, Comparison of intact neuronal signature enrichment in gray matter spot transcriptomes of MS patients (n = 73,182) compared to controls (n = 10,096). Statistical significance assessed by an unpaired two-tailed t-test. The exact p value is 2.22e-308. **c**, Mean intact neuronal signature enrichment (Intact neuronal sign. enr.) of n = 174 gray matter sampling regions plotted separately by donor identity. **d**, Mapping of intact neuronal signature enrichment values onto gray matter.

Fig. 2: Neurodegeneration involves distinct biological processes across interacting cell types.

a, Graphical representation of spatial gene co-expression analysis. **b**, Gene co-expression network of *n* = 174 sampling regions in the gray matter. Nodes represent genes, edges indicate co-expression. Modules with more than 100 genes were downsampled for visual clarity. **c**, Predicted cell-type expression for genes in b. **d–f**, Relationship between enrichment of the intact neuronal signature and summarized module expression (module eigengene values) based on *n* = 156 MS sampling regions. Underlying data shown as dot plot, data points exceeding y axis limits displayed on plot edge. Intact (MS GM intact) and degenerating MS gray matter (MS GM degen.) are indicated. **d,** Modules downregulated with progressing neurodegeneration. **e**, Modules unchanged with progressing neurodegeneration. **f**, Modules upregulated with progressing neurodegeneration. **g**, Projection of module eigengene values onto gray matter in comparison to enrichment of the intact neuronal signature.

Fig. 3: High sensitivity proteomics validates biological processes associated with MS neurodegeneration on the protein level. a, Graphical summary of spatial proteomics. **b**, Overlap between genes / proteins detected in the spatial transcriptomics and proteomics data sets. **c**, Intact neuronal signature enrichment in proteomic data for *n* = 56 MS and *n* = 9 control samples. **d**, Comparison between transcriptome and proteome for modules associated with neurodegeneration. *n* = 4,093 jointly detected genes / proteins are plotted. Correlation coefficients based on Pearson correlations.

Fig. 4: A spatially resolved ligand-receptor interactome reveals trophic factor deprivation and deregulated inflammatory processes.

a, Graphical summary of ligand-receptor co-expression analysis. **b**, Categorization of gray matter sampling regions into control (*n* = 18), intact MS gray matter (*n* = 111) and degenerating MS gray matter (*n* = 45), based on intact neuronal signature enrichment. FDR-adjusted unpaired two-sided t-tests. **c**, Representative example of predicting ligand–receptor interaction by spatially resolving expression of matching binding partners. See e for region localization. **d**, Heatmap summarizing scaled expression of significantly (FDR-adjusted

unpaired two-sided t-tests, p value ≤ 0.1) up- or down-regulated interactions between non-MS control gray matter (Contr. GM, *n* = 18) and intact MS gray matter (MS GM intact, *n* = 111) and tracking of the same interactions in degenerating MS gray matter (MS GM degen., *n* = 45). **e**,**i**, Representative projections of spatially co-expressed ligand-receptor interactions for indicated groups. **e**, *GAS6–TYRO3* exemplifying anti-inflammatory interactions. *C3–C3AR1* exemplifying pro-inflammatory interactions. **i**, *BMP4–BMPR1B_BMPR2* exemplifying trophic interactions downregulated in intact MS GM intact. *WNT5A–FZD1* exemplifying trophic interactions upregulated in intact MS GM intact. **f**,**j,** Quantification of interactions shown in e and i for *n* = 18 non-MS control tissue regions, *n* = 111 intact MS gray matter regions and *n* = 45 degenerating MS gray matter regions. FDR-adjusted unpaired two-sided t-tests. **g**,**k**, Correlation of interactions highlighted in e and i with intact neuronal signature reduction of *n* = 156 MS gray matter samples. FDR-adjusted p values and correlation coefficients based on two-sided Pearson correlations. Exact *p* value for *GAS6–TYRO3* = 1.75e-24. Exact *p* value for *WNT5A–FZD1* = 4.11e-21 **h**,**l**, Mean expression of all trophic and inflammation-associated interactions in indicated groups based on the same samples as used in f.

Fig. 5: Trophic factor deprivation and inflammatory interactions are connected in multifaceted intercellular communication networks.

a, Schematic representation of cell type deconvolution for ligand / receptor co-expression. **b**, UMAP plot depicting integrated human brain snRNA-seq data. **c**, Representative example of spatial association between ligand–receptor expression and cell type distribution. **d–f**, Cell type prediction scores for all ligand–receptor interactions from Fig. 4d. **g–i**, Chord diagrams summarizing intercellular communications via ligand–receptor interactions. Cell types with prediction scores above the 90th percentile are shown. Chord color indicates the ligand-providing cell type.

Fig. 6: Multiple animal models support the mechanistic involvement of MS ligand–receptor candidates in CNS-damage.

a, Graphical summary of assessing mechanistic involvement of candidate LR gene sets in neurodegeneration using an shRNA-based genome-wide *in vivo* screen for essential CNS genes[45]. **b**, Graphical summary of assessing the effects of candidate gene perturbations on published *in vivo* CNS disease models. AD, Alzheimer's disease; ALS, amyotrophic lateral sclerosis; EAE, experimental autoimmune encephalitis; PD, Parkinson's disease; TBI, traumatic brain injury. All search queries and identified perturbations are listed in Supplementary Table 5. **c**, Assessment of mechanistic involvement of candidate genes in neurodegeneration as shown in a. The X-axis represents the fraction of genes in each gene set that were identified as essential CNS genes in Wertz et al.[45]. The Y-axis depicts the mean phenotype strength for each gene set, i.e. the degree to which knockdown of these genes led to depletion of CNS cells. Gray data points represent 10,000 ligand–receptor gene sets randomly selected from all input ligand–receptor genes with the same mean set size as for the candidate gene sets. Moderate jittering is applied to the random data to avoid overplotting. Confidence ellipses are drawn to indicate gene sets that are significantly enriched for essential CNS genes including the candidate gene sets. Experiment based on *n* = 86 C57Bl/6 mice treated with stereotactic injections of shRNA-carrying lentiviruses into both striata. **d**, Assessment of the mechanistic effect of specific perturbations of candidate genes on 7 different *in vivo* models for CNS diseases as shown in b. The number of experiments in favor of CNS protection is plotted for indicated genes with negative values representing experiments, in which the gene contributed to an exacerbation of the disease model. Experiments in which perturbation of candidate genes showed no effect are included in the *n* number indicated on the left. Net effects across all experiments for one candidate gene are color-coded as indicated in the legend.

Fig. 7: Prioritizing new therapeutic targets to broadly address mechanisms of neurodegeneration in progressive MS.

a, Graphical summary of prioritization approach for therapeutic targets. **b**, Mean absolute correlation coefficient for each candidate interaction and all co-expression modules (*n* = 156

MS gray matter samples). 95%-bootstrap confidence intervals are shown centered around mean absolute module correlations. Modules are separated by vertical lines within bars. **c**, Comparison of mean absolute module correlation between pro-inflammatory (*n* = 15), anti-inflammatory (*n* = 15) and trophic (*n* = 19) ligand–receptor interactions. Box plot centered on median, bounds defined between the 25th and 75th percentile with minimum and maximum defined as median ± 1.5 x interquartile range and whiskers extending to the lowest / highest value within this range. FDR-adjusted unpaired two-sided t-tests. **d**, CNS-specificity of each receptor plotted in relation to mean absolute module correlation (*n* = 16,704 RNA-sequencing samples from 52 tissues of 948 donors)[48]. **e**–**h**, Expression of indicated receptors in GTEx human post mortem tissues. Tissue (sub-)categories are represented on the x-axis in alphabetical order. For tissues used see methods. **i**–**l**, Immunohistochemistry of indicated proteins in representative tissues. Image credit: Human Protein Atlas[49]. For image URLs see Supplementary Table 6.

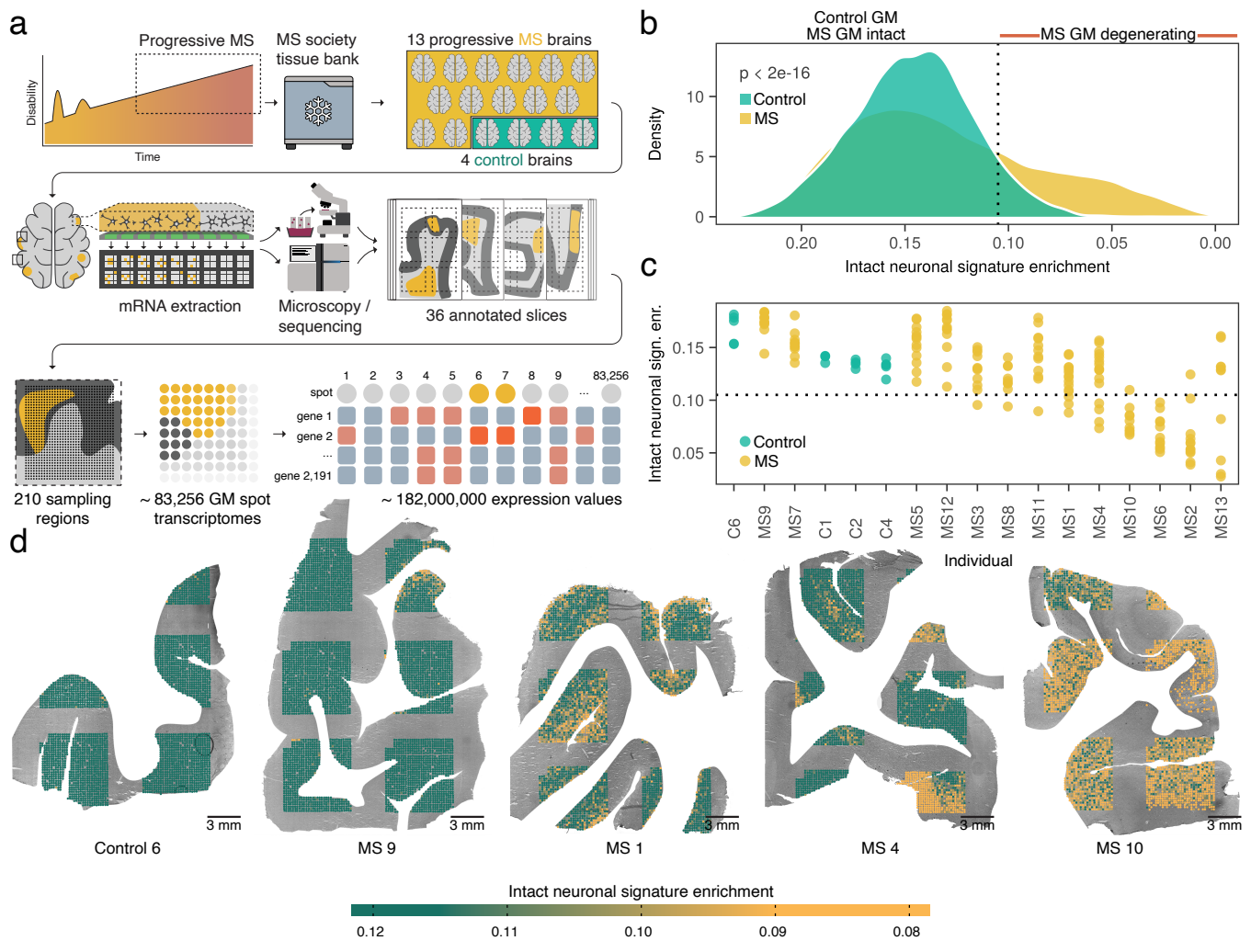
a
Progressive MS
Disability
Time
MS society tissue bank
13 progressive MS brains
4 control brains
mRNA extraction
Microscopy / sequencing
36 annotated slices
210 sampling regions
~ 83,256 GM spot transcriptomes
spot
gene 1
gene 2
gene 2,191
83,256
~ 182,000,000 expression values
b
Control GM
MS GM intact
MS GM degenerating
p < 2e-16
Control
MS
Density
Intact neuronal signature enrichment
c
Intact neuronal sign. enr.
Control
MS
C6
MS9
MS7
C1
C2
C4
MS5
MS12
MS3
MS8
MS11
MS1
MS4
MS10
MS6
MS2
MS13
Individual
d
3 mm
Control 6
MS 9
MS 1
MS 4
MS 10
Intact neuronal signature enrichment
0.12
0.11
0.10
0.09
0.08

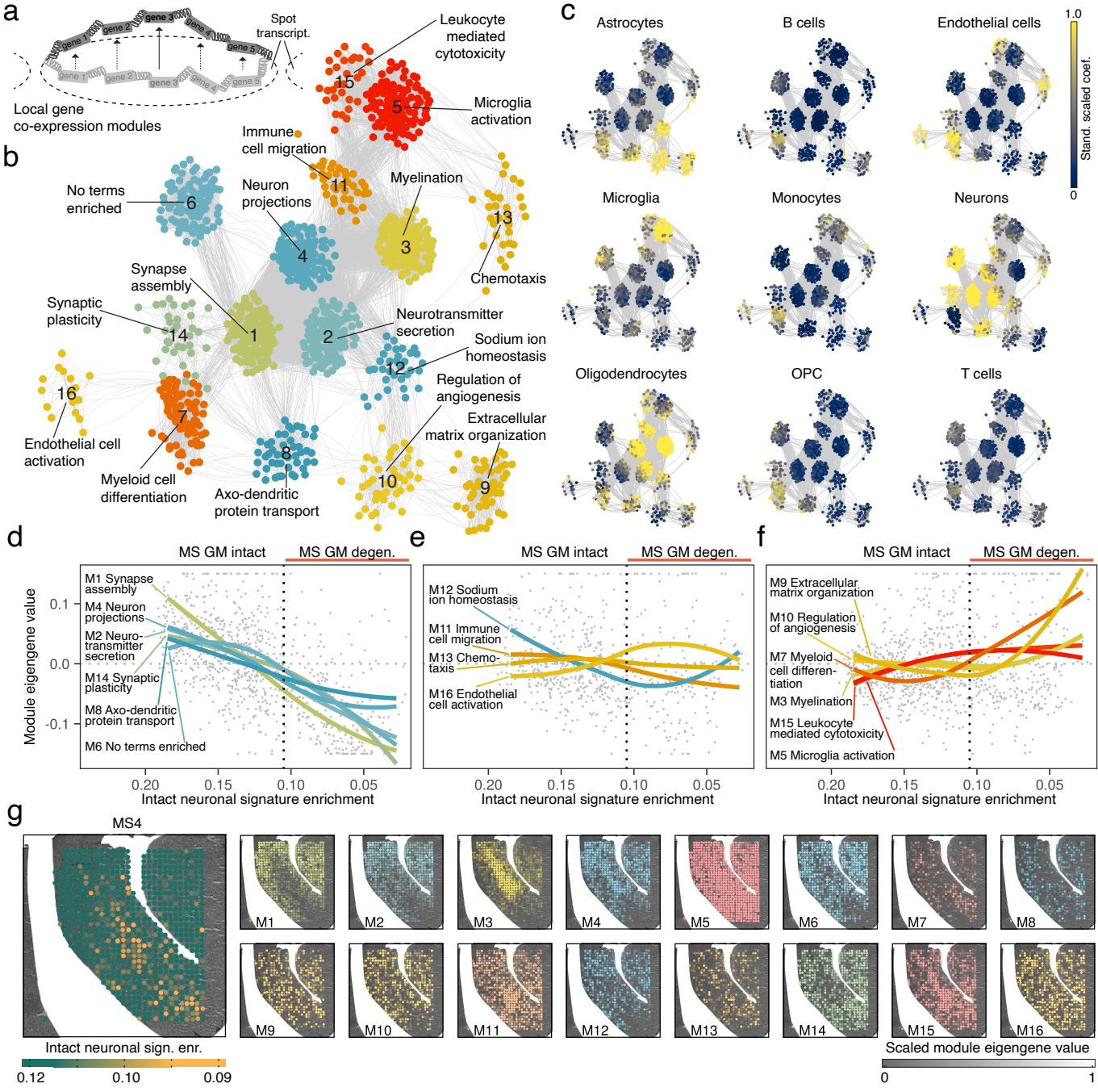
a
Spot transcript.
Local gene co-expression modules
b
Leukocyte mediated cytotoxicity
Microglia activation
Immune cell migration
Neuron projections
Myelination
No terms enriched
Synapse assembly
Synaptic plasticity
Chemotaxis
Neurotransmitter secretion
Sodium ion homeostasis
Regulation of angiogenesis
Extracellular matrix organization
Endothelial cell activation
Myeloid cell differentiation
Axo-dendritic protein transport
c
Astrocytes
B cells
Endothelial cells
Microglia
Monocytes
Neurons
Oligodendrocytes
OPC
T cells
Stand. scaled coef.
d
MS GM intact
MS GM degen.
Module eigengene value
M1 Synapse assembly
M4 Neuron projections
M2 Neuro-transmitter secretion
M14 Synaptic plasticity
M8 Axo-dendritic protein transport
M6 No terms enriched
Intact neuronal signature enrichment
e
M12 Sodium ion homeostasis
M11 Immune cell migration
M13 Chemo-taxis
M16 Endothelial cell activation
f
M9 Extracellular matrix organization
M10 Regulation of angiogenesis
M7 Myeloid cell differen-tiation
M3 Myelination
M15 Leukocyte mediated cytotoxicity
M5 Microglia activation
g
MS4
Intact neuronal sign. enr.
Scaled module eigengene value

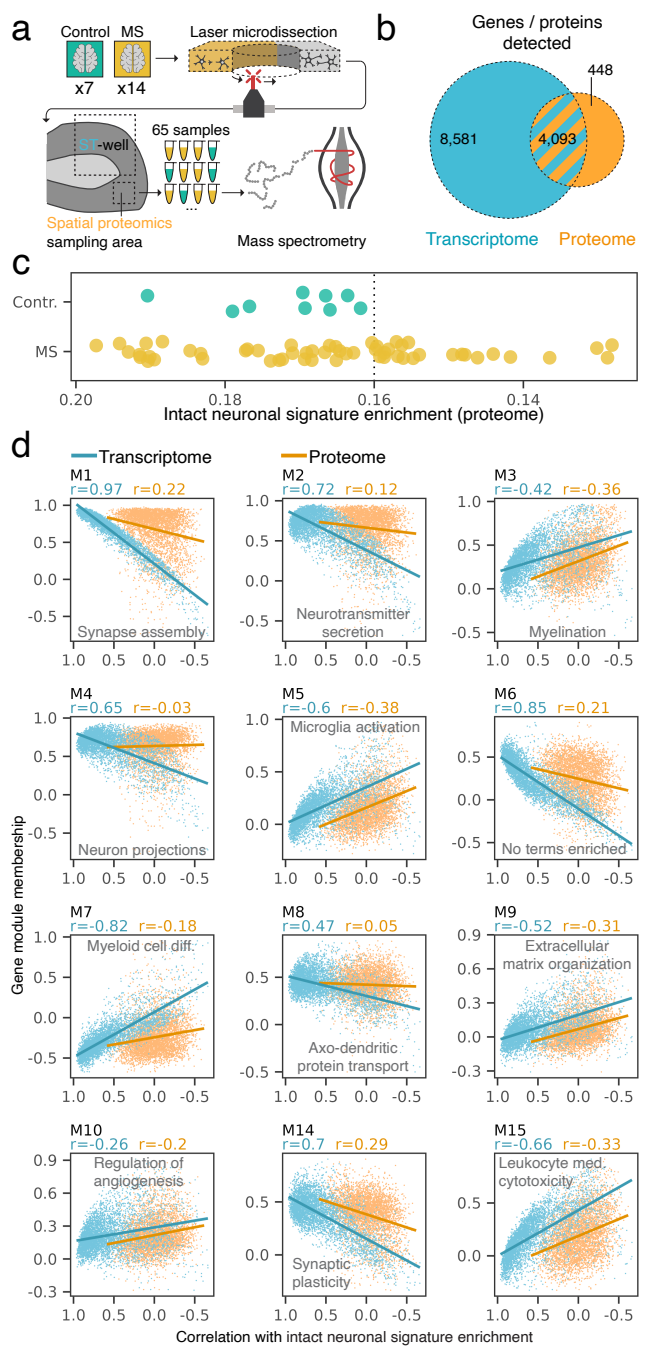
a
Control
MS
x7
x14
Laser microdissection
65 samples
ST-well
Spatial proteomics
sampling area
Mass spectrometry
b
Genes / proteins
detected
448
8,581
4,093
Transcriptome
Proteome
c
Contr.
MS
0.20
0.18
0.16
0.14
Intact neuronal signature enrichment (proteome)
d
Transcriptome
Proteome
M1
r=0.97 r=0.22
Synapse assembly
M2
r=0.72 r=0.12
Neurotransmitter
secretion
M3
r=-0.42 r=-0.36
Myelination
M4
r=0.65 r=-0.03
Neuron projections
M5
r=-0.6 r=-0.38
Microglia activation
M6
r=0.85 r=0.21
No terms enriched
M7
r=-0.82 r=-0.18
Myeloid cell diff.
M8
r=0.47 r=0.05
Axo-dendritic
protein transport
M9
r=-0.52 r=-0.31
Extracellular
matrix organization
M10
r=-0.26 r=-0.2
Regulation of
angiogenesis
M14
r=0.7 r=0.29
Synaptic
plasticity
M15
r=-0.66 r=-0.33
Leukocyte med.
cytotoxicity
Gene module membership
Correlation with intact neuronal signature enrichment

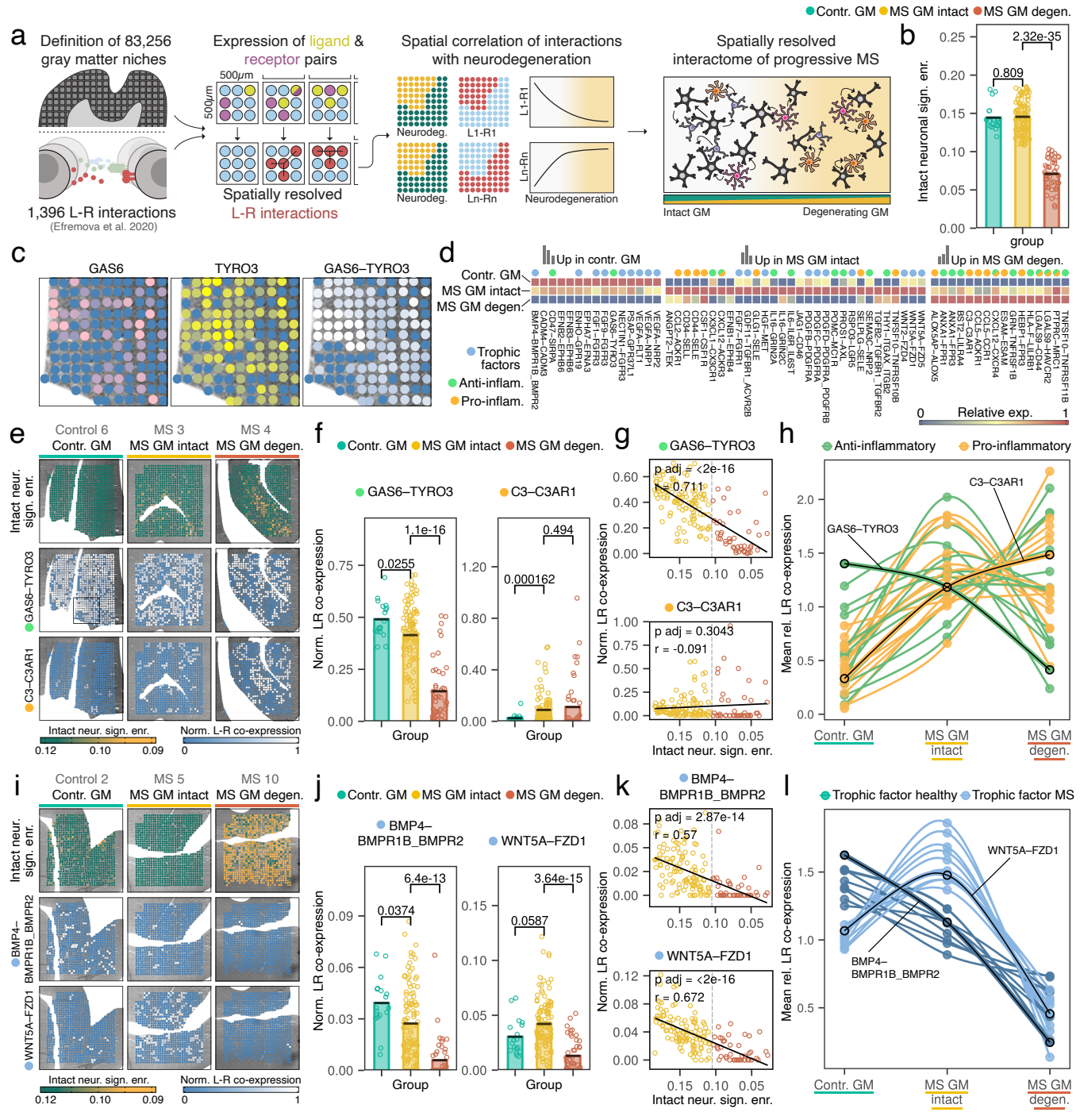
Contr. GM
MS GM intact
MS GM degen.
a
Definition of 83,256 gray matter niches
1,396 L-R interactions
(Efremova et al. 2020)
Expression of ligand & receptor pairs
500μm
Spatially resolved L-R interactions
Spatial correlation of interactions with neurodegeneration
Neurodeg.
L1-R1
Ln-Rn
Spatially resolved interactome of progressive MS
Intact GM
Degenerating GM
b
Intact neuronal sign. enr.
2.32e-35
0.809
group
c
GAS6
TYRO3
GAS6–TYRO3
d
Up in contr. GM
Up in MS GM intact
Up in MS GM degen.
Contr. GM
MS GM intact
MS GM degen.
Trophic factors
Anti-inflam.
Pro-inflam.
Relative exp.
e
Control 6
Contr. GM
MS 3
MS GM intact
MS 4
MS GM degen.
Intact neur. sign. enr.
GAS6–TYRO3
C3–C3AR1
Norm. L-R co-expression
f
Contr. GM
MS GM intact
MS GM degen.
GAS6–TYRO3
C3–C3AR1
Norm. LR co-expression
1.1e-16
0.0255
0.494
0.000162
Group
g
GAS6–TYRO3
p adj = <2e-16
r = 0.711
C3–C3AR1
p adj = 0.3043
r = -0.091
Norm. LR co-expression
Intact neur. sign. enr.
h
Anti-inflammatory
Pro-inflammatory
GAS6–TYRO3
C3–C3AR1
Mean rel. LR co-expression
Contr. GM
MS GM intact
MS GM degen.
i
Control 2
Contr. GM
MS 5
MS GM intact
MS 10
MS GM degen.
Intact neur. sign. enr.
BMP4–BMPR1B_BMPR2
WNT5A–FZD1
Norm. L-R co-expression
j
Contr. GM
MS GM intact
MS GM degen.
BMP4–BMPR1B_BMPR2
WNT5A–FZD1
Norm. LR co-expression
6.4e-13
0.0374
3.64e-15
0.0587
Group
k
BMP4–BMPR1B_BMPR2
p adj = 2.87e-14
r = 0.57
WNT5A–FZD1
p adj = <2e-16
r = 0.672
Norm. LR co-expression
Intact neur. sign. enr.
l
Trophic factor healthy
Trophic factor MS
WNT5A–FZD1
BMP4–BMPR1B_BMPR2
Mean rel. LR co-expression
Contr. GM
MS GM intact
MS GM degen.

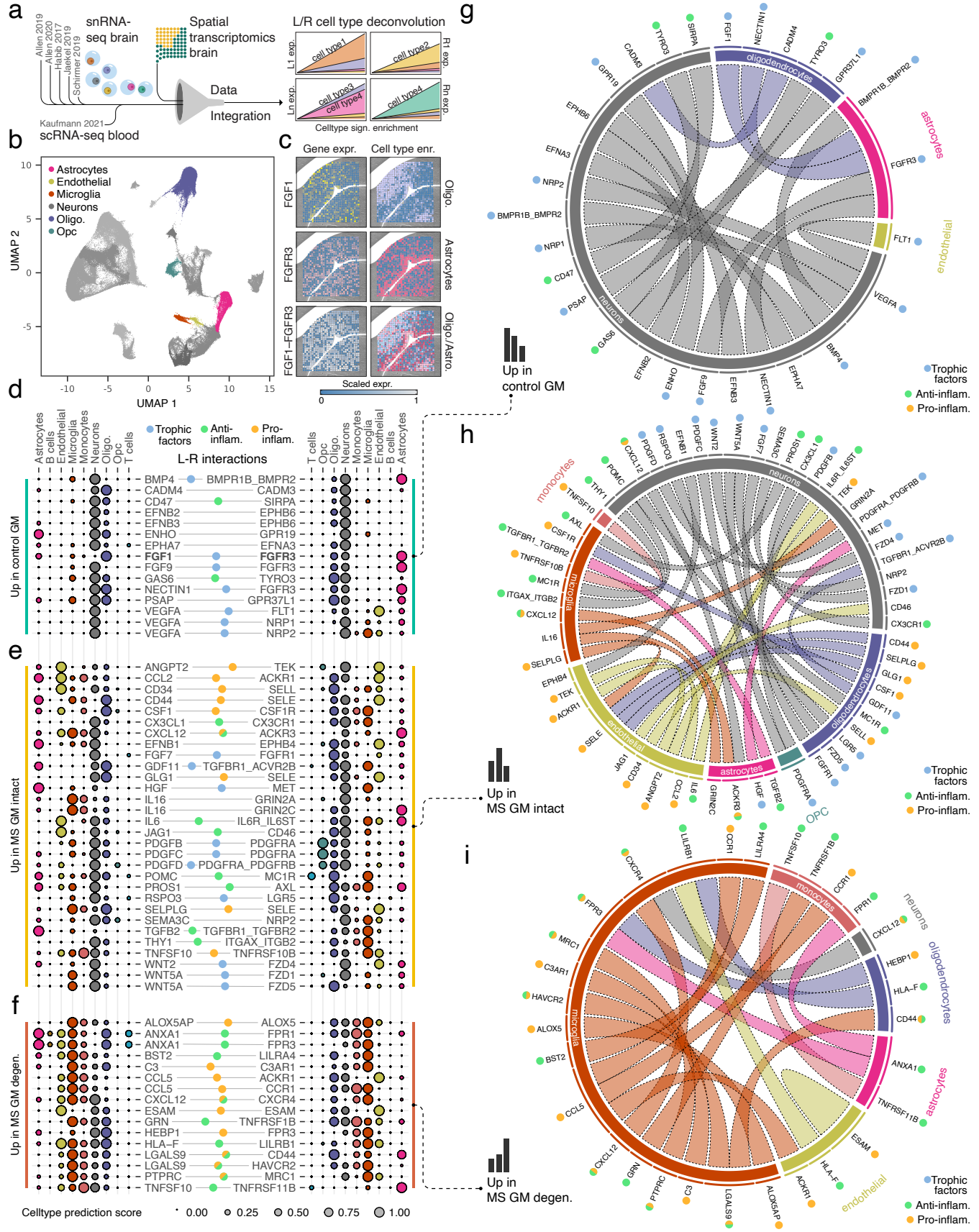
a
snRNA-seq brain
Allen 2019
Allen 2020
Habib 2017
Jaekel 2019
Schirmer 2019
Kaufmann 2021
scRNA-seq blood
Spatial transcriptomics brain
Data Integration
L/R cell type deconvolution
cell type1
cell type2
cell type3
cell type4
L1 exp.
R1 exp.
Ln exp.
Rn exp.
Celltype sign. enrichment
b
Astrocytes
Endothelial
Microglia
Neurons
Oligo.
Opc
UMAP 1
UMAP 2
c
Gene expr.
Cell type enr.
FGF1
FGFR3
FGF1–FGFR3
Oligo.
Astrocytes
Oligo./Astro.
Scaled expr.
d
Trophic factors
Anti-inflam.
Pro-inflam.
L-R interactions
Up in control GM
BMP4 BMPR1B_BMPR2
CADM4 CADM3
CD47 SIRPA
EFNB2 EPHB6
EFNB3 EPHB6
ENHO GPR19
EPHA7 EFNA3
FGF1 FGFR3
FGF9 FGFR3
GAS6 TYRO3
NECTIN1 FGFR3
PSAP GPR37L1
VEGFA FLT1
VEGFA NRP1
VEGFA NRP2
e
Up in MS GM intact
ANGPT2 TEK
CCL2 ACKR1
CD34 SELL
CD44 SELE
CSF1 CSF1R
CX3CL1 CX3CR1
CXCL12 ACKR3
EFNB1 EPHB4
FGF7 FGFR1
GDF11 TGFBR1_ACVR2B
GLG1 SELE
HGF MET
IL16 GRIN2A
IL16 GRIN2C
IL6 IL6R_IL6ST
JAG1 CD46
PDGFB PDGFRA
PDGFC PDGFRA
PDGFD PDGFRA_PDGFRB
POMC MC1R
PROS1 AXL
RSPO3 LGR5
SELPLG SELE
SEMA3C NRP2
TGFB2 TGFBR1_TGFBR2
THY1 ITGAX_ITGB2
TNFSF10 TNFRSF10B
WNT2 FZD4
WNT5A FZD1
WNT5A FZD5
f
Up in MS GM degen.
ALOX5AP ALOX5
ANXA1 FPR1
ANXA1 FPR3
BST2 LILRA4
C3 C3AR1
CCL5 ACKR1
CCL5 CCR1
CXCL12 CXCR4
ESAM ESAM
GRN TNFRSF1B
HEBP1 FPR3
HLA–F LILRB1
LGALS9 CD44
LGALS9 HAVCR2
PTPRC MRC1
TNFSF10 TNFRSF11B
Celltype prediction score
0.00
0.25
0.50
0.75
1.00
g
oligodendrocytes
astrocytes
endothelial
neurons
Up in control GM
h
monocytes
microglia
neurons
oligodendrocytes
astrocytes
endothelial
Up in MS GM intact
i
OPC
monocytes
microglia
neurons
oligodendrocytes
astrocytes
endothelial
Up in MS GM degen.

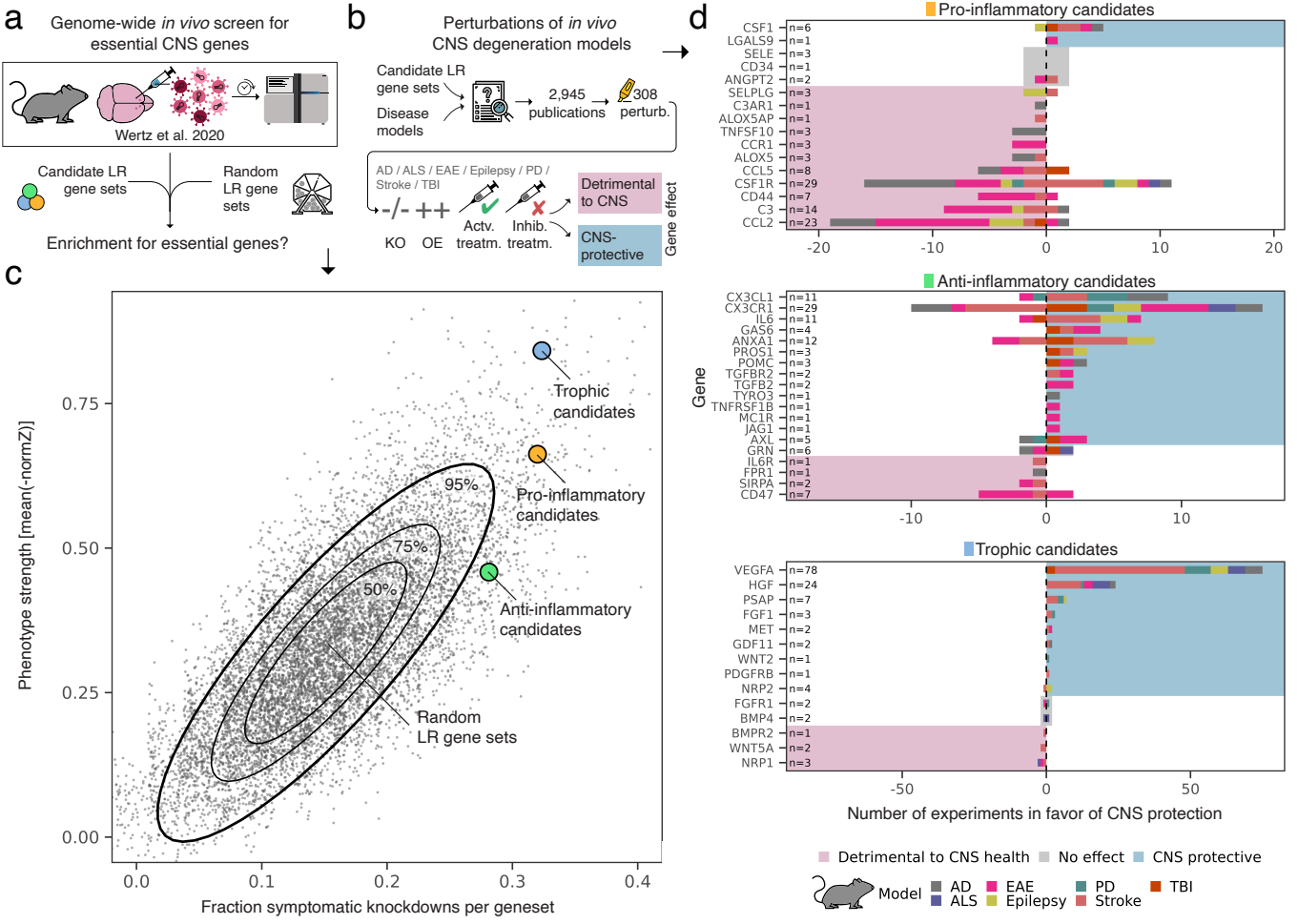
a
Genome-wide *in vivo* screen for essential CNS genes
Wertz et al. 2020
Candidate LR gene sets
Random LR gene sets
Enrichment for essential genes?
b
Perturbations of *in vivo* CNS degeneration models
Candidate LR gene sets
Disease models
2,945 publications
308 perturb.
AD / ALS / EAE / Epilepsy / PD / Stroke / TBI
-/- ++
KO
OE
Actv. treatm.
Inhib. treatm.
Detrimental to CNS
CNS-protective
Gene effect
c
Phenotype strength [mean(-normZ)]
Fraction symptomatic knockdowns per geneset
95%
75%
50%
Trophic candidates
Pro-inflammatory candidates
Anti-inflammatory candidates
Random LR gene sets
d
Pro-inflammatory candidates
CSF1 n=6
LGALS9 n=1
SELE n=3
CD34 n=1
ANGPT2 n=2
SELPLG n=3
C3AR1 n=1
ALOX5AP n=1
TNFSF10 n=3
CCR1 n=3
ALOX5 n=3
CCL5 n=8
CSF1R n=29
CD44 n=7
C3 n=14
CCL2 n=23
Anti-inflammatory candidates
Gene
CX3CL1 n=11
CX3CR1 n=29
IL6 n=11
GAS6 n=4
ANXA1 n=12
PROS1 n=3
POMC n=3
TGFBR2 n=2
TGFB2 n=2
TYRO3 n=1
TNFRSF1B n=1
MC1R n=1
JAG1 n=1
AXL n=5
GRN n=6
IL6R n=1
FPR1 n=1
SIRPA n=2
CD47 n=7
Trophic candidates
VEGFA n=78
HGF n=24
PSAP n=7
FGF1 n=3
MET n=2
GDF11 n=2
WNT2 n=1
PDGFRB n=1
NRP2 n=4
FGFR1 n=2
BMP4 n=2
BMPR2 n=1
WNT5A n=2
NRP1 n=3
Number of experiments in favor of CNS protection
Detrimental to CNS health
No effect
CNS protective
Model
AD
ALS
EAE
Epilepsy
PD
Stroke
TBI

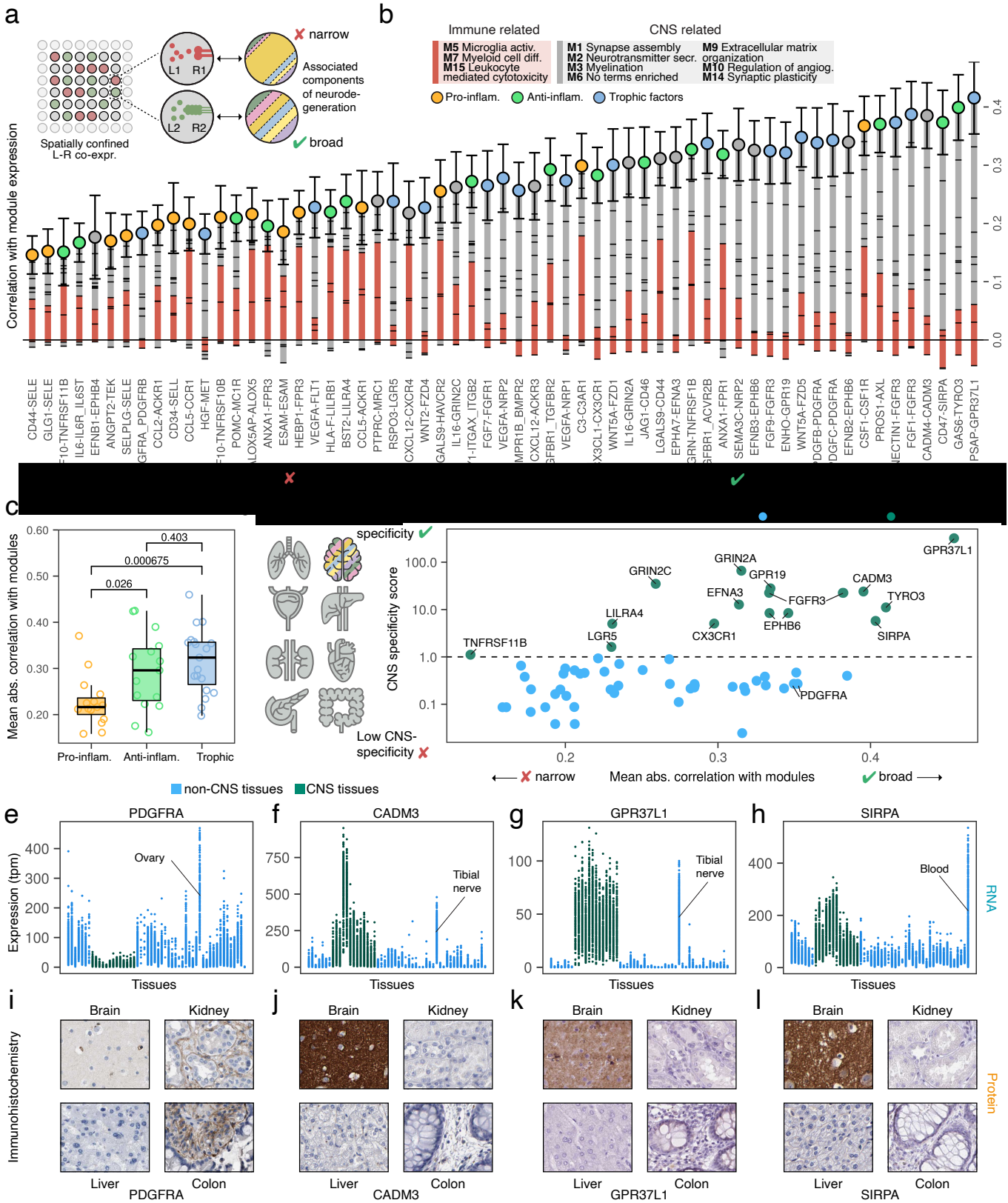
a
L1
R1
L2
R2
narrow
Associated components of neurode-generation
broad
Spatially confined L-R co-expr.
b
Immune related
M5 Microglia activ.
M7 Myeloid cell diff.
M15 Leukocyte mediated cytotoxicity
CNS related
M1 Synapse assembly
M2 Neurotransmitter secr.
M3 Myelination
M6 No terms enriched
M9 Extracellular matrix organization
M10 Regulation of angiog.
M14 Synaptic plasticity
Pro-inflam.
Anti-inflam.
Trophic factors
Correlation with module expression
CD44-SELE
GLG1-SELE
IL6-IL6R_IL6ST
EFNB1-EPHB4
ANGPT2-TEK
SELPLG-SELE
PDGFRB
CCL2-ACKR1
CD34-SELL
CCL5-CCR1
HGF-MET
POMC-MC1R
ANXA1-FPR3
ESAM-ESAM
HEBP1-FPR3
VEGFA-FLT1
HLA-F-LILRB1
BST2-LILRA4
CCL5-ACKR1
PTPRC-MRC1
RSPO3-LGR5
CXCL12-CXCR4
WNT2-FZD4
GALS9-HAVCR2
IL16-GRIN2C
FGF7-FGFR1
VEGFA-NRP2
MPR1B_BMPR2
CXCL12-ACKR3
VEGFA-NRP1
C3-C3AR1
WNT5A-FZD1
IL16-GRIN2A
JAG1-CD46
LGALS9-CD44
EPHA7-EFNA3
ANXA1-FPR1
SEMA3C-NRP2
EFNB3-EPHB6
FGF9-FGFR3
ENHO-GPR19
WNT5A-FZD5
PDGFB-PDGFRA
PDGFC-PDGFRA
EFNB2-EPHB6
CSF1-CSF1R
PROS1-AXL
FGF1-FGFR3
CADM4-CADM3
CD47-SIRPA
GAS6-TYRO3
PSAP-GPR37L1
c
Mean abs. correlation with modules
0.403
0.000675
0.026
Pro-inflam.
Anti-inflam.
Trophic
specificity
Low CNS-specificity
CNS specificity score
GPR37L1
GRIN2A
GRIN2C
GPR19
CADM3
EFNA3
FGFR3
TYRO3
LILRA4
EPHB6
CX3CR1
SIRPA
LGR5
TNFRSF11B
PDGFRA
narrow
Mean abs. correlation with modules
broad
non-CNS tissues
CNS tissues
e
PDGFRA
Ovary
f
CADM3
Tibial nerve
g
GPR37L1
Tibial nerve
h
SIRPA
Blood
Expression (tpm)
Tissues
RNA
i
j
k
l
Brain
Kidney
Liver
Colon
Immunohistochemistry
Protein
PDGFRA
CADM3
GPR37L1
SIRPA

References

1. Dendrou, C. A., Fugger, L. & Friese, M. A. Immunopathology of multiple sclerosis. *Nat Rev Immunol* **15**, 545–558 (2015).

2. Tintore, M., Vidal-Jordana, A. & Sastre-Garriga, J. Treatment of multiple sclerosis — success from bench to bedside. *Nat Rev Neurol* **15**, 53–58 (2019).

3. Carassiti, D. *et al.* Neuronal loss, demyelination and volume change in the multiple sclerosis neocortex. *Neuropath Appl Neuro* **44**, 377–390 (2018).

4. Scalfari, A. *et al.* The cortical damage, early relapses, and onset of the progressive phase in multiple sclerosis. *Neurology* **90**, e2107–e2118 (2018).

5. Magliozzi, R. *et al.* A Gradient of neuronal loss and meningeal inflammation in multiple sclerosis. *Ann Neurol* **68**, 477–493 (2010).

6. Wegner, C., Esiri, M. M., Chance, S. A., Palace, J. & Matthews, P. M. Neocortical neuronal, synaptic, and glial loss in multiple sclerosis. *Neurology* **67**, 960–967 (2006).

7. Ontaneda, D., Fox, R. J. & Chataway, J. Clinical trials in progressive multiple sclerosis: lessons learned and future perspectives. *Lancet Neurology* **14**, 208–223 (2015).

8. Kappos, L. *et al.* Siponimod versus placebo in secondary progressive multiple sclerosis (EXPAND): a double-blind, randomised, phase 3 study. *Lancet* **391**, 1263–1273 (2018).

9. Montalban, X. *et al.* Ocrelizumab versus Placebo in Primary Progressive Multiple Sclerosis. *New Engl J Medicine* **376**, 209–220 (2017).

10. Longo, S. K., Guo, M. G., Ji, A. L. & Khavari, P. A. Integrating single-cell and spatial transcriptomics to elucidate intercellular tissue dynamics. *Nat Rev Genet* 1–18 (2021) doi:10.1038/s41576-021-00370-8.

11. Ståhl, P. L. *et al.* Visualization and analysis of gene expression in tissue sections by spatial transcriptomics. *Science* **353**, 78–82 (2016).

12. Coscia, F. *et al.* A streamlined mass spectrometry–based proteomics workflow for large-scale FFPE tissue analysis. *J Pathology* **251**, 100–112 (2020).

13. Mann, M. The ever expanding scope of electrospray mass spectrometry—a 30 year journey. *Nat Commun* **10**, 3744 (2019).

14. Habib, N. *et al.* Massively parallel single-nucleus RNA-seq with DroNc-seq. *Nat Methods* **14**, 955–958 (2017).

15. Hodge, R. D. *et al.* Conserved cell types with divergent features in human versus mouse cortex. *Nature* **573**, 61–68 (2019).

16. Jäkel, S. *et al.* Altered human oligodendrocyte heterogeneity in multiple sclerosis. *Nature* **566**, 543–547 (2019).

17. Schirmer, L. *et al.* Neuronal vulnerability and multilineage diversity in multiple sclerosis. *Nature* **573**, 75–82 (2019).

18. Kaufmann, M. *et al.* Identifying CNS-colonizing T cells as potential therapeutic targets to prevent progression of multiple sclerosis. *Med* **2**, 296-312.e8 (2021).

19. Efremova, M., Vento-Tormo, M., Teichmann, S. A. & Vento-Tormo, R. CellPhoneDB: inferring cell–cell communication from combined expression of multi-subunit ligand–receptor complexes. *Nat Protoc* **15**, 1484–1506 (2020).

20. Han, M. H. *et al.* Janus-like opposing roles of CD47 in autoimmune brain inflammation in humans and mice. *J Exp Medicine* **209**, 1325–1334 (2012).

21. Lisak, R. P. & Benjamins, J. A. Melanocortins, Melanocortin Receptors and Multiple Sclerosis. *Brain Sci* **7**, 104 (2017).

22. Maimone, D., Guazzi, G. C. & Annunziata, P. IL-6 detection in multiple sclerosis brain. *J Neurol Sci* **146**, 59–65 (1997).

23. McCandless, E. E. *et al.* Pathological Expression of CXCL12 at the Blood-Brain Barrier Correlates with Severity of Multiple Sclerosis. *Am J Pathology* **172**, 799–808 (2008).

24. Moll, N. M. *et al.* Imaging Correlates of Leukocyte Accumulation and CXCR4/CXCL12 in Multiple Sclerosis. *Arch Neurol-chicago* **66**, 44–53 (2009).

25. Trebst, C. *et al.* CCR1+/CCR5+ Mononuclear Phagocytes Accumulate in the Central Nervous System of Patients with Multiple Sclerosis. *Am J Pathology* **159**, 1701–1710 (2001).

26. Morrissey, M. A., Kern, N. & Vale, R. D. CD47 Ligation Repositions the Inhibitory Receptor SIRPA to Suppress Integrin Activation and Phagocytosis. *Immunity* **53**, 290-302.e6 (2020).

27. Rothlin, C. V., Ghosh, S., Zuniga, E. I., Oldstone, M. B. A. & Lemke, G. TAM Receptors Are Pleiotropic Inhibitors of the Innate Immune Response. *Cell* **131**, 1124–1136 (2007).

28. Cao, W. *et al.* Regulation of TLR7/9 responses in plasmacytoid dendritic cells by BST2 and ILT7 receptor interaction. *J Exp Medicine* **206**, 1603–1614 (2009).

29. Persson, G., Jørgensen, N., Nilsson, L. L., Andersen, L. H. J. & Hviid, T. V. F. A role for both HLA-F and HLA-G in reproduction and during pregnancy? *Hum Immunol* **81**, 127–133 (2019).

30. Cardona, A. E. *et al.* Control of microglial neurotoxicity by the fractalkine receptor. *Nat Neurosci* **9**, 917–924 (2006).

31. Carrera Silva, E. A. *et al.* T Cell-Derived Protein S Engages TAM Receptor Signaling in Dendritic Cells to Control the Magnitude of the Immune Response. *Immunity* **39**, 160–170 (2013).

32. Michael, J., Marschallinger, J. & Aigner, L. The leukotriene signaling pathway: a druggable target in Alzheimer's disease. *Drug Discov Today* **24**, 505–516 (2019).

33. Reis, E. S., Mastellos, D. C., Hajishengallis, G. & Lambris, J. D. New insights into the immune functions of complement. *Nat Rev Immunol* **19**, 503–516 (2019).

34. Meyer, R. C., Giddens, M. M., Coleman, B. M. & Hall, R. A. The protective role of prosaposin and its receptors in the nervous system. *Brain Res* **1585**, 1–12 (2014).

35. Cable, D. M. *et al.* Robust decomposition of cell type mixtures in spatial transcriptomics. *Nat Biotechnol* 1–10 (2021) doi:10.1038/s41587-021-00830-w.

36. Dong, R. & Yuan, G.-C. SpatialDWLS: accurate deconvolution of spatial transcriptomic data. *Genome Biol* **22**, 145 (2021).

37. Elosua-Bayes, M., Nieto, P., Mereu, E., Gut, I. & Heyn, H. SPOTlight: seeded NMF regression to deconvolute spatial transcriptomics spots with single-cell transcriptomes. *Nucleic Acids Res* **49**, e50–e50 (2021).

38. Chitu, V., Gokhan, Ş., Nandi, S., Mehler, M. F. & Stanley, E. R. Emerging Roles for CSF-1 Receptor and its Ligands in the Nervous System. *Trends Neurosci* **39**, 378–393 (2016).

39. Tang, W. *et al.* TRAIL receptor mediates inflammatory cytokine release in an NF-κB-dependent manner. *Cell Res* **19**, 758–767 (2009).

40. Nibbs, R. J. B. & Graham, G. J. Immune regulation by atypical chemokine receptors. *Nat Rev Immunol* **13**, 815–829 (2013).

41. Souma, T. *et al.* Context-dependent functions of angiopoietin 2 are determined by the endothelial phosphatase VEPTP. *Proc National Acad Sci* **115**, 201714446 (2018).

42. Zöller, T. *et al.* Silencing of TGFβ signalling in microglia results in impaired homeostasis. *Nat Commun* **9**, 4011 (2018).

43. Migeotte, I. *et al.* Identification and characterization of an endogenous chemotactic ligand specific for FPRL2. *J Exp Medicine* **201**, 83–93 (2005).

44. Tang, W. *et al.* The Growth Factor Progranulin Binds to TNF Receptors and Is Therapeutic Against Inflammatory Arthritis in Mice. *Science* **332**, 478–484 (2011).

45. Wertz, M. H. *et al.* Genome-wide In Vivo CNS Screening Identifies Genes that Modify CNS Neuronal Survival and mHTT Toxicity. *Neuron* **106**, 76-89.e8 (2020).

46. Lehrman, E. K. *et al.* CD47 Protects Synapses from Excess Microglia-Mediated Pruning during Development. *Neuron* **100**, 120-134.e6 (2018).

47. Toth, A. B. *et al.* Synapse maturation by activity-dependent ectodomain shedding of SIRPα. *Nat Neurosci* **16**, 1417–1425 (2013).

48. GTEx-Consortium. The GTEx Consortium atlas of genetic regulatory effects across human tissues. *Science* **369**, 1318–1330 (2020).

49. Uhlén, M. *et al.* Tissue-based map of the human proteome. *Science* **347**, 1260419 (2015).

50. Spiegel, I. *et al.* A central role for Necl4 (SynCAM4) in Schwann cell–axon interaction and myelination. *Nat Neurosci* **10**, 861–869 (2007).

51. Golan, N. *et al.* Genetic Deletion of Cadm4 Results in Myelin Abnormalities Resembling Charcot-Marie-Tooth Neuropathy. *J Neurosci* **33**, 10950–10961 (2013).

52. Jolivalt, C. G., Vu, Y., Mizisin, L. M., Mizisin, A. P. & Calcutt, N. A. Impaired Prosaposin Secretion During Nerve Regeneration in Diabetic Rats and Protection of Nerve Regeneration by a Prosaposin-Derived Peptide. *J Neuropathology Exp Neurology* **67**, 702–710 (2008).

53. Golde, T. E. The therapeutic importance of understanding mechanisms of neuronal cell death in neurodegenerative disease. *Mol Neurodegener* **4**, 8 (2009).

54. Evans, S. R. *et al.* A Randomized Trial Evaluating Prosaptide™ for HIV-Associated Sensory Neuropathies: Use of an Electronic Diary to Record Neuropathic Pain. *Plos One* **2**, e551 (2007).

55. Taylor, E. M., Otero, D. A., Banks, W. A. & O'Brien, J. S. Retro-inverso prosaptide peptides retain bioactivity, are stable In vivo, and are blood-brain barrier permeable. *J Pharmacol Exp Ther* **295**, 190–4 (2000).

56. Xie, Y. *et al.* FGF/FGFR signaling in health and disease. *Signal Transduct Target Ther* **5**, 181 (2020).

57. Jin, K. *et al.* Cerebral neurogenesis is induced by intranasal administration of growth factors. *Ann Neurol* **53**, 405–409 (2003).

58. Russ, A. *et al.* Blocking "don't eat me" signal of CD47-SIRPα in hematological malignancies, an in-depth review. *Blood Rev* **32**, 480–489 (2018).

Methods

Study cohort

Fresh-frozen brain tissue from MS patients or non-MS / non-neurological controls for spatial RNA-sequencing and proteomics was obtained from the UK Multiple Sclerosis Society Tissue Bank (registered charity 207495). This project falls under the umbrella of ethical approval obtained by the MS Society Tissue Bank (08/MRE09/31+5) and the MS Society Tissue Bank ensured informed consent was obtained by participants. Donor characteristics of all human tissue donors are summarized in Supplementary Table 1. The requirements for inclusion of samples into the study cohort were a minimum RNA integrity number (RIN) of 6, a limited postmortem interval before sampling (<= 30 h) and no other competing diagnoses of brain diseases except for MS. In addition to our cohort size being in line with other spatial transcriptomics studies[59,60], the number of patient samples relative to controls was proportionately increased to address the substantial spatial heterogeneity that was expected between sampling areas within and across patients.

Spatial transcriptomics

Spatial transcriptomics were performed following the protocol of the original spatial transcriptomics publication[11]. Briefly, cryosections of MS and control brain tissues were cut to a thickness of 10 µm and adhered to Library Preparation (LP) glass slides purchased from Spatial Transcriptomics, Stockholm, Sweden. Each slide ('chip') contained 6 sampling regions measuring 6.5 mm x 6.9 mm. One sampling region consisted of 1,007 spatially barcoded mRNA-capturing spots. The spots had a diameter of 100 µm and were arranged at a center-to-center distance of 200 µm. Tissue adherence to chips was followed by HE staining and image acquisition, tissue permeabilization (1% Triton X followed by 0.1% pepsin, Sigma-Aldrich) and overnight in situ cDNA synthesis. Tissues were then removed using Proteinase K solution (Qiagen), followed by cDNA cleavage using a mix of Second Strand Buffer (1.1X)

(Thermo Fisher Scientific), dNTPs (8.75 µM each) (Thermo Fisher Scientific), BSA (0.20 µg/µl) (NEB) and USER enzyme (0.1 U/µl) (NEB). The cleaved cDNA was collected and immediately stored at -20°C until further processing. Visualization of spots for alignment with HE images was achieved by hybridization with Cy3-labelled surface probes (IDT) (Supplementary Table 7), followed by fluorescence image acquisition. Brightfield and fluorescent images were manually aligned using the ST Spot Detector tool described previously [61] on the basis of structural features detectable in both. Library preparation was carried out using a 2-phase robotic pipetting system (Magnatrix 8000+ Workstation, Magnetic Biosolutions AB) as described previously [62]. The robot was loaded with the following reagent mixtures. In phase 1 for second strand synthesis: First Strand Buffer (2.7X) (Thermo Fisher Scientific), DNA polymerase I (3.7 U/µl) (Thermo Fisher Scientific), RNase H (0.18 U/µl) (Thermo Fisher Scientific); for end blunting reaction: T4 DNA polymerase (3 U/µl) (NEB), EDTA (80 mM) (Thermo Fisher Scientific); for in vitro transcription: T7 NTP mix (7.5 mM each), T7 reaction buffer (1X), T7 enzyme mix (1X) (all part of Ambion MEGAscript T7 kit, Thermo Fisher Scientific), SUPERaseIn (1 U/µl) (Thermo Fisher Scientific). In phase 2 for adapter ligation: aRNA ligation adapter (0.71 µM) (IDT) (Supplementary Table 7), T4 RNA Ligase Reaction Buffer (1X) (NEB), T4 RNA Ligase 2, truncated (20 U/µl) (NEB), RNase Inhibitor, murine (4 U/µl) (NEB), for second cDNA synthesis: reverse transcription primer (1.7 µM) (IDT) (Supplementary Table 7), First Strand Buffer (2.5X) (Thermo Fisher Scientific), dNTP mix (0.83 mM each) (Thermo Fisher Scientific), DTT (12.5 mM) (Thermo Fisher Scientific), RNaseOut Recombinant Ribonuclease Inhibitor (5 U/µl) (Thermo Fisher Scientific), Superscript III (25 U/µl) (Thermo Fisher Scientific). Between all steps, libraries were purified using Agencourt RNAClean XP Beads (Beckman Coulter) as described previously [62]. Library indices were added with a PCR reaction. The number of cycles needed for indexing the libraries was determined by qPCR reaction in a total volume of 10 µl containing Kapa HiFi HotStart Ready Mix (1X) (Roche), EvaGreen (1X) (Biotium), PCR Primer InPE1.0 (0.5 µM) (IDT) (Supplementary Table 7), PCR Primer InPE2.0 (0.01 µM) (IDT) (Supplementary Table 7), 0.5 µM PCR Index (IDT) (Supplementary Table 7) and 2 µl of purified cDNA. The following

qPCR protocol was used: 98°C for 3 mins, followed by 25 cycles of 98°C for 20 sec, 60°C for 30 sec, 72°C for 30 sec. Once the number of cycles needed for indexing each library was determined, libraries were indexed in a total reaction volume of 25 µl (5 µl cDNA + 20 µl reaction mix as above). The 6 libraries obtained from each ST slide were indexed with PCR indices 1-6 or 7-12 (Supplementary Table 7). After indexing PCR, libraries were purified using Agencourt AMPure XP beads (Beckman Coulter) according to the manufacturer's protocol. The ratio of bead to sample volume used was 1.25:1. 80% ethanol was used for the wash steps. The libraries were eluted in 20 µl RNase/DNase-free water. The average fragment length of the libraries was determined using a DNA High-Sensitivity kit (Agilent) and Bioanalyzer 2100 according to the manufacturer's protocol. The cDNA concentration was measured by Qubit dsDNA HS assay (Thermo Fisher Scientific) according to the manufacturer's protocol. For sequencing, the 6 libraries from a slide were diluted to 4nM or 2nM (depending on the starting concentration of the least concentrated sample), pooled and prepared for paired-end sequencing (R1 30bp, R2 55bp) on the Illumina NextSeq 550 platform (Illumina) according to the manufacturer's protocol.

Spatial transcriptomics data processing

All software versions, references and availability are indicated in Supplementary Table 8. Raw data processing was performed with the Spatial Transcriptomics pipeline and using the GRCh38 reference genome. Further data processing and quality control was performed in the programming language R. Spot transcriptome count matrices were cleaned and filtered as follows. Non-protein coding genes and ribosomal protein coding genes were removed, as well as spot transcriptomes consisting of less than 300 expressed genes. Sampling areas retaining less than 20 spot transcriptomes meeting the quality criteria were excluded from further analysis. Count matrices were normalized and scaled using the Seurat functions *NormalizeData* and *ScaleData* with standard parameters[63,64]. Separate HE images from each sampling region were stitched together in Adobe Photoshop and spot coordinates were

transferred into a joint coordinate system for each chip. Structural annotation of microscopy images was performed based on neuropathologic assessment by adding vector masks for each feature of interest including gray matter, white matter, perimeningeal and empty areas to yield pixel-precise spatial metadata for all images. Each spot transcriptome was then annotated automatically according to its position on the annotated image. For a focused analysis of gray matter neurodegeneration, white matter, perimeningeal and empty areas were excluded from the downstream analysis and blocked out in microscopy images for visual clarity. The final data set consisted of 174 gray matter sampling regions with overall detection of 12,674 genes out of which an average 1,800 genes were quantifiable per spot transcriptome.

Integration with single cell data

To facilitate cell type deconvolution of spot transcriptomes, spatial transcriptomics data was integrated with snRNA-seq data of human cortical brain tissue from five different sources including reference data from the Allen brain atlas[14–17] and scRNA-seq data of blood immune cells[18]. Data integration was performed using enrichment score-based deconvolution[10] implemented with DEseq2[65] and AUCell[66]. DEseq2 was employed to identify cell type-specific marker signatures in the single cell data and AUCell to test for the enrichment of each signature in all spot transcriptomes. A detailed description of this methodology is provided in the section ‘Tracking of neurodegeneration’ for the example of neurons and was performed in analogous fashion for all other cell types.

To validate the robustness of the applied enrichment score-based deconvolution, alternative integration methods, designed for the purpose of integration of single cell and spatial transcriptomics data, were also performed (see Extended Data Fig. 5). Specifically, Robust Cell Type Decomposition (RCTD)[35], spatial Dampened Weighted Least Squares (spatialDWLS)[36] and SPOTlight[37] were performed.

RCTD was applied as implemented in the spacexr package and was run according to the official documentation. In brief, a ‘single cell reference object’ was created from cortical brain snRNA-seq data (further described in the methods section ‘Tracking of neurodegeneration’) with the *Reference* function. For each sampling region spatial transcriptomics data was loaded separately into a ‘SpatialRNA object’ using the *SpatialRNA* function. Next, an ‘RCTD object’ was created with default parameters for each sampling region using the single cell reference object and ‘SpatialRNA object’ as inputs. RCTD was performed by running the *run.RCTD* function with doublet_mode set to ‘full’. Resulting RCTD scores for each spot transcriptome were extracted from the RCTD object and saved in a joined dataframe for all sampling regions.

SpatialDWLS was applied as implemented in the Giotto package and was run according to the official documentation. In brief, cell type markers were extracted from single cell data using DEseq2 as described in the methods section ‘Tracking of neurodegeneration’. Mean expression of all marker genes was calculated for each cell type in the single cell data using the *rowMeans* function. For each sampling region spatial transcriptomics data was loaded separately into a ‘Giotto object’ using the *createGiottoObject* function. The data was then processed by consecutively running the Giotto functions *normalizeGiotto* (with default parameters), *calculateHVG* (with default parameters), *runPCA* (with genes limited to highly variable genes determined with *calculateHVG*), *signPCA* (with genes limited to highly variable genes determined with *calculateHVG*), *createNearestNetwork* (with dimensions_to_use set to 10 and k set to 10) and *doLeidenCluster* (with resolution set to 0.4 and n_interations set to 1000). Finally, DWLS was performed by applying the *runDWLSDeconv* function to the Giotto object using a matrix of the mean expression of all celltype marker genes in the single cell data as input for the sign_matrix parameter and with cutoff set to 0. Resulting spatialDWLS scores for each spot transcriptome were extracted from the Giotto object and saved in a joined dataframe for all sampling regions.

SPOTlight was applied as implemented in the SPOTlight package and was run according to the official documentation. In brief, an existing ‘Seurat object’ of the single cell data (see the methods section ‘Tracking of neurodegeneration’) was downsampled to 100 cells for each cell type without replacement. Highly variable genes were identified by applying the Seurat function *FindVariableFeatures* with default parameters. From another ‘Seurat object’, containing the spatial transcriptomics data, spot transcriptomes from each sampling region were sequentially extracted and SPOTlight was applied to them. For this purpose, the *SPOTlight* function was run for the single cell data and each sampling region of the spatial transcriptomics data, both supplied to the function as ‘Seurat objects’ and with the groups argument set to the cell type identities, mgs set to the raw DEseq2 results of the differential gene expression analysis between cell types in the single cell data (see the methods section ‘Tracking of neurodegeneration’), hvg set to the highly variable genes identified with *FindVariableFeatures* and weight_id set to the log2FoldChange column of the DEseq2 results. SPOTlight scores for each spot transcriptome were extracted from the resulting object and saved in a joined dataframe for all sampling regions.

To determine overall concordance between the different integration methods tested, the results of scoring each cell type by each method on all spot transcriptomes were compared with each other in a correlation matrix using Pearson correlation. To test the robustness of enrichment score-based deconvolution more specifically, cell type scores for all spot transcriptomes were plotted as scatter plots for enrichment score-based deconvolution in direct comparison with each alternative method; r and p values were derived using Pearson correlation and p values were FDR-adjusted. The overall strong correlation between all methods tested was visualized by a representative projection of spot deconvolution results for all four integration methods onto tissue.

Spatial proteomics

For spatial proteomics, fresh frozen brain samples were cryo-sectioned into 10 µm sections. Tissue sections were mounted on polyethylene naphthalate (PEN) membrane slides (ThermoFisher) in preparation for laser capture microdissection (LCM) and transferred back to -80°C storage before further processing. Immediately prior to micro-dissection, each individual LCM slide was retrieved from storage and stained with HE. LCM was performed on a laser pressure catapulting micro-dissection microscope (PALM Microbeam, Zeiss). Gray matter areas were chosen for sampling manually by referring to HE-stained tissue morphology. Laser-dissected areas were circular (0.05 mm^2), with each completed sample consisting of approximately 120 adjacent circular cuts and a total volume of < 0.06 mm^3. Samples were collected into adhesive caps and transported on dry ice for subsequent proteomics analysis. Collected tissue was transferred in 100 µl lysis buffer (300 mM Tris/HCl pH8, 50% 2,2,2-trifluoroethanol) into 0.2 ml PCR tubes for further processing. After controlled heating (to avoid cap opening from overpressure) for 90 min at 90°C, samples were sonicated in a Bioruptor (15 cycles, duty cycle 50%). Samples were then vacuum-dried for approximately 1 h at 60°C until 20 µl remained. DTT was added to a final concentration of 5 mM and incubated for 20 min at room temperature. 20 mM CAA were added for alkylation and incubated for another 20 min at room temperature. LC-grade water was added to adjust the sample volume to 100 µl and tryptic digestion started by the addition of LysC and Trypsin at an enzyme to protein ratio of 1:100. Samples were digested overnight at 37°C at 1400 rpm. The next day, TFA was added to 1% final concentration (v/v) to stop digestion. Peptide clean-up was carried out by stage tipping. Details of the entire workflow can be found in our recent publication[12]. Nanoflow LC–MS analysis of tryptic peptides was conducted on a quadrupole orbitrap mass spectrometer (Q Exactive HF-X, Thermo Fisher Scientific, Bremen, Germany) coupled to an EASY nLC 1200 ultra-high-pressure system (Thermo Fisher Scientific) via a nano-electrospray ion source. About 300 ng of peptides were loaded on a 50 cm HPLC-column (75 µm inner diameter, New Objective, Woburn, MA, USA; in-house packed using

ReproSil-Pur C18-AQ 1.9-µm silica beads; Dr Maisch GmbH, Ammerbuch, Germany) and measured over a total gradient length of 100 min with increasing buffer B (80% acetonitrile [ACN] and 0.1% formic acid; Merck, Darmstadt, Germany) concentration. The mass spectrometer was operated in data independent acquisition (DIA) mode. The DIA method consisted of one MS1 scan (350 or 300 to 1,650 m/z, resolution 60,000 or 120,000, maximum injection time 60 ms, AGC target 3E6) and 32 segments at varying isolation windows from 14,4 m/z to 562,8 m/z (resolution 30,000, maximum injection time 54 ms, AGC target 3E6). Stepped normalized collision energy was 25, 27.5 and 30. The default charge state for MS2 was set to 2.

Spatial proteomics data processing

DIA raw files were analyzed with the Spectronaut Pulsar X software under default settings for direct DIA analysis. The human UniProtKB database (2019) was used as the target database. Proteins identified based on a single peptide were filtered out, as well as decoy hits and proteins not passing the default quantification criteria (Q-value cut-off 0.01). In order to enable a direct comparison between our spatial transcriptomics and proteomics data, peptide mapping was carried out in an isotype-agnostic fashion. Thus, each detected protein could be mapped unambiguously to one gene if also present in the spatial transcriptomics data set. Proteins were filtered for those that could be quantified in at least 70% of all samples and samples were excluded, where more than 300 of these proteins were not quantifiable. The final data set consisted of 4,541 proteins measured in 65 cortical gray matter samples; the transcripts for 4,093 of these proteins were also detected on the RNA level in our spatial transcriptomics data set.

Tracking of neurodegeneration

In order to systematically measure the distribution of neurodegeneration in spatial transcriptomics and proteomics data of MS gray matter a consensus signature was prepared

that marked intact neurons in brain tissue. In brief, differential gene expression analyses between cell populations in snRNA-seq data of cortical brain tissue were performed to identify genes, which are exclusively expressed by healthy neurons. Measuring enrichment of this marker gene set in gray matter spot transcriptomes from both controls and MS patients served to identify areas where the healthy neuronal signal was reduced relative to the control samples and to quantify the degree of change. In detail, snRNA-seq data of non-MS / non-neurological post mortem brain tissue was first integrated from five different sources including reference data from the Allen brain atlas[14–17]. All data sets were filtered for transcriptomes consisting of a minimum of 300 detected genes, normalized using SCtransform[63] and integrated based on cross data set anchors[64] by consecutive execution of the Seurat functions *SelectIntegrationFeatures*, *PrepSCTIntegration*, *FindIntegrationAnchors* and *IntegrateData*. Unsupervised transcriptomic clusters were identified with a shared nearest neighbor (SNN) modularity optimization-based algorithm implemented in Seurat and cell types annotated based on reference annotations from the two Allen brain atlas data sets. Based on this integrated data set and scRNA-seq data of blood immune cells[18], neuronal transcriptomes and non-neuronal transcriptomes were compared to identify a signature exclusively marking neuronal populations. Specifically, for each donor 1,000 transcriptomes were sampled with replacement from each cell type and aggregated to pseudo-bulks. Next, DEseq2[65] was run with *betaPrior* set to *TRUE* and using "~celltype" as design formula. Neurons were contrasted with other cells by applying the DEseq2 *results* functions to the resulting object and giving each non-neuronal cell type equal negative weights using the "listValues" parameter. An analogous process was performed also for each non-neuronal cell type in contrast to the remaining cell types and neurons to determine their marker signatures. The resulting list of differentially expressed genes was then further consolidated by filtering on genes detected in at least 0.1% of transcriptomes of the spatial transcriptomics data set and genes, where the foldchange between non-neuronal cells and neurons was higher than the foldchange in any other cell type comparison. The final intact neuronal signature was comprised of the top 100 differentially expressed genes (FDR-adjusted p value ≤ 0.05) discriminating between neurons

and non-neuronal cell populations as ranked by the difference in foldchange for this comparison and the second highest foldchange of any other cell type. The specificity and the discriminatory properties of the derived signature were validated through gene set enrichment analysis on the pseudo-bulked cortical snRNA-seq data as well as scRNA-seq data of peripheral immune cells using the *AUCell_calcAUC* function from the AUCell package[66] with the "aucMaxRank" parameter set to 10% of the number of detected genes in the data set (Extended Data Fig. 1). Enrichment of the derived intact neuronal signature was then calculated in the same fashion for each spot transcriptome in the spatial transcriptomics data set as well as for each proteome of the spatial proteomics data set. In both cases signature enrichment extended to low values in MS samples not observed in non-MS controls validating the ability of this approach to systematically track and quantify a reduction of intact neurons termed neurodegeneration in the analyzed tissue. For visualization purposes enrichment of the intact neuronal signature was represented on a color scale and plotted for each spot transcriptome at the mapped coordinates on HE-stained microscopy images. To confirm that a reduction of the intact neuronal signature was indicative of tissue lesions, neuropathologic assessment was performed on cryosections adjacent to sections used for spatial transcriptomics. For this purpose, 10 µm cryosections were stained with anti-MOG supernatant (1:50 dilution, kindly gifted by Prof R. Reynolds, Imperial College London) and Oil Red O powder (Raymond A Lamb Ltd).

Gene co-expression analysis

Modules of spatially co-expressed genes were determined by performing a weighted correlation network analysis (WGCNA)[67,68] on the aggregated expression data of all sampling regions (n = 174). For this purpose, the *blockwiseModules* function from the WGCNA R package was employed with "power" set to 12, "minModuleSize" set to 20 and "deepSplit" to 4. The resulting co-expression network was transformed into an igraph object[69] using the *wgcna2igraph* function from the limmaDE2 package. For visualization purposes modules with

more than 100 genes were randomly downsampled (without replacement). A community-based layout was applied to the network before plotting using the ggraph package. For module annotation, GO term enrichment analysis was performed on the genes of each module using the *enrichGO* function from the clusterProfiler package[70] with the parameter "ont" (ontology) set to "BP" (biological processes), "minGSSize" (minimum size of GO terms to consider) set to 10 and the "universe" parameter set to all input genes of the WGCNA analysis. Uniquely enriched GO terms with an FDR-adjusted p value ≤ 0.1 were selected for each module. Highly redundant terms were consolidated based on semantic similarities using the *simplify* function from clusterProfiler. The remaining significant GO terms for each module were represented as GO term enrichment maps using clusterProfilers *emapplot* function and exported to Cytoscape[71] for plotting (Extended Data Fig. 3). Summary annotation labels for each module that broadly represented the enriched terms were derived from supervised inspection of the enrichment maps. To model cell specific gene expression based on integration with single cell data (see section 'Integration with single cell data'), a linear model for each gene was then calculated with an expression formula analogous to "gene expression ~ signature enrichment cell type 1 + signature enrichment cell type 2 + … + signature enrichment cell type n". The resulting coefficients were standardized and scaled for each gene and visualized by mapping them onto the gene co-expression network. In order to track gene modules over the course of neurodegeneration the *moduleEigengenes* function of WGCNA was used to derive summarized expression values for each module in all of n = 174 aggregated sampling regions. The resulting module expression data was then put into relation to the enrichment of the intact neuronal signature for each sampling region. Locally estimated scatterplot smoothing (LOESS) curve fitting was applied to generate regression curves for each module and similar patterns of regulation were grouped for visualization. Additionally, for cross-modality comparison with the spatial proteomics data set, a module membership value was determined for each gene that had a matching protein in the proteomics data set. Module membership was defined according to the WGCNA package as the concordance between expression of each gene and the expression of each module defined on a continuous scale instead of

discrete assignment of genes to individual modules. Furthermore, the Pearson correlation between each gene and the enrichment of the intact neuronal signature was determined. The relationship between module membership and correlation with neuronal signature enrichment was thus informative as to whether genes correlated with neurodegeneration were also correlated (or anti-correlated) to specific modules and could be compared across modalities.

Ligand–receptor interactome

Spatial co-expression analysis of matching ligand and receptor pairs was based on information from cellphoneDB[19]. First, the expression of each ligand and each receptor listed in cellphoneDB was determined for each spot transcriptome in the data set. For ligands or receptors assembled from multiple subunits, expression was defined as the expression of the subunit that was least expressed in a spot. If one of the required subunits was not detected, the expression of the entire complex was set to 0 for this location. Next, the expression of matching ligands and receptors was assessed for each spot transcriptome and its directly neighboring spots. Thus, for each ligand-receptor interaction it was determined if for a given spot that expresses partner A, partner B is expressed in the same location or in one of the (maximum 8) surrounding spots. Matching pairs co-expressed in the same location or in two directly neighboring spots (i.e within 200 µm of one another) were considered to have a high probability of interaction and a joined 'interaction expression' value was derived defined as the average between the mean expression of partner A and the mean expression of partner B for the given spot transcriptome and its direct neighbors. In order to relate the occurrence of these interactions to neurodegeneration, sampling regions were assigned to one of three groups ('control gray matter', 'intact MS gray matter', 'degenerating MS gray matter'). The distinction between 'intact MS gray matter' and 'degenerating MS gray matter' was based on intact neuronal signature enrichment aggregated for each sampling region, where 'intact' areas had enrichment values ≥ 0.105 defining the lower boundary of the enrichment in controls and 'degenerating' areas values below this cutoff (Fig. 1B and C). To determine interactions

significantly altered between control areas and intact MS gray matter, unpaired two-sided t-tests were performed between the respective groups (n = 18 control gray matter and n = 111 intact MS gray matter). P values were FDR-adjusted for the number of comparisons and interactions with adjusted p values ≤ 0.1 considered to be significant. Additionally, for significant interactions Pearson correlations with the enrichment of the intact neuronal signature were determined and FDR-adjusted unpaired two-sided t-tests were calculated for the comparison between intact and degenerating MS gray matter. Literature research was carried out for all significant interactions to verify the evidence supporting a given ligand–receptor pairing and to annotate them functionally (Supplementary Table 4). In the process interactions were filtered out that were only supported by large-scale protein interaction screens and lacked replication in independent experiments. Formal orphan G-protein coupled receptors were retained when several publications supported a ligand pairing. The mean expression of interactions annotated as growth factors, anti-inflammatory or pro-inflammatory stimuli was plotted for control regions, intact and degenerating MS gray matter to uncover overall regulation patterns for these processes. To demonstrate the underlying data for this summary analysis, expression values for representative interactions were plotted for all sampling regions and their regulation was visualized on the tissue. To integrate the derived ligand–receptor interactome with cell type information, the expression of each ligand and receptor was modeled based on the enrichment of cell type marker signatures derived from snRNA-seq datasets. A detailed description of how the applied cell type marker signatures were extracted and the cell type modeling was performed is provided in previous sections (‘Integration with single cell data’, ‘Tracking of neurodegeneration’ and ‘Gene co-expression analysis’). Cell type prediction scores for all interactions were visualized as bubble charts created in ggplot and chord diagrams created with the circlize package[72].

Multimodal reproducibility of the regulation of ligand–receptor interactions between MS intact GM and control areas was assessed by referring to the high sensitivity proteomics data set. In identical fashion to the RNA data, a cut-off for the intact neuronal signature enrichment was

defined for the protein data, which separated samples with a neuronal signal comparable to control tissue (MS GM intact) from samples with abnormally low enrichment (MS GM degenerating) (compare dotted line in Fig. 3c). Thus, for all ligand/receptor genes also detected on the protein level, the expression in MS GM intact could be compared to control areas. Log2-fold changes were calculated for both RNA and protein expression and their concordance assessed using a Pearson correlation.

Evaluation of age and sex bias for ligand–receptor analysis

To test, whether the sex- and age-disbalance between the MS and control cohorts (Supplementary Table 1) biased the results of the ligand–receptor co-expression analysis, post mortem cortical brain tissue samples of n = 336 donors from the GTEx consortium[48] were analyzed, for which gender and age group were known. A linear model was determined for all detected genes of the human genome, which predicted gene expression in the human cortex dependent on age and sex as interacting variables. The following model formula was used in R:

$$Cortical\ gene\ expression \sim age * sex$$

Which is equivalent to the notation

$$Cortical\ gene\ expression \sim age + sex + age{:}\,sex$$

As a result, the variance explained by age and sex in the human cortex (adjusted R^2 of the model) as well as its significance (adjusted p value of the model ≤ 0.1) was determined for each gene. The relative fraction of significantly age-/sex-biased genes was compared between differentially co-expressed ligand–receptor genes and the genome as a reference. For ligand/receptor genes with significant bias, the directionality (e.g. increased in males, increased with age) was extracted based on the sign of the respective model coefficients. On this basis, suspected bias patterns were analyzed, such as a potential enrichment of genes with bias towards younger females in the set of genes increased in MS patients.

Mechanistic *in vivo* validation

To assess whether perturbation of candidate ligand–receptor genes impact the survival of CNS cells, in particular neurons, data from an *in vivo* genome-wide shRNA knockdown screen in the striata of wild type C57BL/6 mice[45] was employed. Briefly, in this study, essential CNS genes were identified by measuring the depletion of CNS cells carrying a specific knockdown at two different time points (four weeks and seven months after lentiviral introduction of shRNA libraries). Statistical assessment was performed using the DrugZ algorithm[73]. See the original publication for further details[45]. Based on this data set, for each set of our candidate genes (pro-inflammatory, anti-inflammatory, trophic) the fraction of genes determined as CNS-essential was calculated, as well as the mean normalized Z-scores for each candidate gene set, which measured the average phenotype strength. Candidate gene sets were then plotted in a coordinate system between the two measures. Statistical significance was tested by comparing candidate gene sets to the distribution of random ligand–receptor gene sets. For this purpose, 10,000 sets of ligand–receptor genes were drawn randomly (with replacement) from the input list of ligand–receptors, with the number of genes per set fixed to the mean number of genes in our candidate sets. For each random set, again the fraction of CNS-essential genes and their average phenotype strength was determined. Confidence ellipses were created for the random data using the *stat_ellipse()* function from the ggplot2 package. Ligand–receptor gene sets outside the 95%-confidence ellipse were determined as significantly different from randomly chosen gene sets and to support the hypothesis that the prioritized genes play a causal role in CNS-health. Note, that the second assumption only holds true for graph areas to the upper right of the 95%-confidence ellipse, which was where all tested candidate gene sets were mapped to.

To systematically assess the mechanistic effect of candidate ligand–receptor genes on a broad range of *in vivo* CNS disease models, a systematic literature research was performed, where specific perturbations of candidate genes were identified and classified. Europe PMC

(https://europepmc.org/), containing all pubmed entries, was queried with the *epmc_search*() function of the europepmc R package. Queries were automatically generated by combining HGNC gene symbols for candidate genes or gene long names determined using the biomaRt package and keywords encoding disease models. The search was limited to titles and abstracts of primary research articles. All building blocks for search queries, as well as the generated queries, are listed in Supplementary Table 5. A total of 2,945 publications were identified and their abstracts extracted using the *epmc_details()* function (Supplementary Table 5). Abstracts were exported to a new line separated json format (jsonl) together with the publication title, the queried candidate gene and the disease model encoded in tags. Abstracts were then read into Doccano as jsonl to perform manual annotation, which was further supported by keyword highlighting with the plugin 'highlight this'. For each publication the following steps were performed and saved in annotation tags: First, evaluation of whether a specific perturbation of the queried candidate gene was performed in the given publication *in vivo*. This included gene knockout or knockdown, gene overexpression, inhibiting treatment (such as blocking antibodies or receptor antagonists) and activating treatment (such as receptor agonists). In cases where the abstract was not sufficiently informative the full-length publication was considered. Secondly, the class of in vivo CNS model used in this perturbation experiment was independently validated. Finally, if the first two conditions were met, the effect of the perturbation on the model outcome was evaluated as either 'amelioration', 'exacerbation' or 'no effect'. As a result, 308 specific *in vivo* perturbations of candidate ligand–receptor genes in CNS disease models were identified and stored in an R dataframe (Supplementary Table 5). Next, the suggested mechanistic effect on CNS-health for each perturbation was determined as follows: Genes were classified as 'detrimental to CNS health' if a reduction of the gene activity (knockout, knockdown, inhibiting treatment) led to an amelioration of the model outcome or an increased activity (overexpression, activating treatment) led to an exacerbation of the model. Vice versa, genes were classified as 'CNS protective' if a reduction of the gene activity (knockout, knockdown, inhibiting treatment) led to an exacerbation of the model outcome or an increased activity (overexpression, activating

treatment) led to an amelioration of the model. Genes, for which perturbation didn't influence the model outcome were classified as 'no effect on CNS health'. This resulted in a tally of published experiments for each candidate gene in favor or against a CNS-protective function (Supplementary Table 5), which was plotted using ggplot2 with indication of contributing classes of *in vivo* CNS models and net effects per gene.

Therapeutic target prioritization

To link the derived ligand–receptor interactome to the annotated gene co-expression modules describing the components of neurodegeneration, Pearson correlations were calculated between the expression of each significant interaction and the summarized expression (eigengene value) of each module. Positive correlation between a module and a given interaction signified high activity of the module in areas, where the ligand and matching receptor were observed frequently in close spatial proximity of one another, whereas anti-correlation indicated the opposite. Based on this relation between ligand–receptor interactions and gene co-expression modules, interactions were prioritized as promising therapeutic targets based on showing greater aggregate connectivity to modules related to neurodegeneration. Specifically, for each interaction the mean absolute correlation with all modules was determined and interactions were ranked by it. To substantiate the robustness of this approach, 95%-bootstrap confidence intervals were calculated by repeating the analysis on 100,000 bootstrap samples. For visualization purposes the relative contributions of each module to the mean absolute module correlation were calculated and stacked to a bar graph color-coded by functional categories. Anti-correlations were indicated by negative values and the overall bar length was scaled to represent the mean absolute module correlation. To further stratify the derived therapeutic targets by their CNS-specificity, the Genotype-Tissue Expression (GTEx) project V8 data set was used comprising post mortem bulk RNA-seq data for many human tissues[48]. After removal of two non-native tissues (cultured fibroblasts and EBV-transformed lymphocytes) n = 16,704 samples from 52 tissues

of 948 donors remained. CNS regions sampled in the data set were amygdala, anterior cingulate cortex (ba24), caudate (basal ganglia), cerebellar hemisphere, cerebellum, cortex, frontal cortex (ba9), hippocampus, hypothalamus, nucleus accumbens (basal ganglia), putamen (basal ganglia), spinal cord (cervical c-1) and substantia nigra. Available non-CNS tissues included adipose - subcutaneous, adipose - visceral (omentum), adrenal gland, aorta, coronary artery, tibial artery, bladder, mammary tissue, ectocervix, endocervix, colon - sigmoid, colon - transverse, gastroesophageal junction, esophageal mucosa, esophageal muscularis, fallopian tube, heart - atrial appendage, heart - left ventricle, kidney - cortex, kidney - medulla, liver, lung, minor salivary gland, skeletal muscle, tibial nerve, ovary, pancreas, pituitary, prostate, skin - not sun exposed (suprapubic), skin - sun exposed (lower leg), small intestine, spleen, stomach, testis, thyroid, uterus, vagina and whole blood. The expression of prioritized receptors was assessed in all available native tissues and averaged for cortical CNS regions and non-CNS tissues. Based on this, a CNS-specificity score was calculated as the ratio between mean cortical expression and mean non-CNS expression supporting the positioning of target receptors in a coordinate system between potential breadth of impact on neurodegeneration (mean absolute module correlation) and exclusivity to the CNS (CNS specificity score). Immunohistochemistry stainings from the human protein atlas[49] (Supplementary Table 6) were evaluated for all available candidate receptors to validate their CNS-enrichment on the protein level. For this purpose, only stainings based on antibodies whose reliability was classified as ‘supported’ or ‘enhanced’ at the time of writing were considered. Brain, kidney, liver and colon were selected as representative organs that had stainings available for all queried proteins.

Quantification and statistical analysis

All statistical analyses performed in this study are described in detail in the respective methods sections including any statistical software used. Software versions, references and availability are indicated in Supplementary Table 8. The exact number of *n* and what *n* represents is

indicated directly in the figure legends for all comparisons in this study and mentioned again in the methods section where applicable. Center, dispersion and precision measures are explained in the figure legends. The statistical test or algorithm to determine statistical significance is indicated both in the figure legends and the respective methods sections for all reported p values. The sample size for this study could not be based on previous data as no other spatial transcriptomics studies on human diseases were available at the time of data acquisition. Thus, the number of samples was maximized within the constraints of available tissue, cost and method throughput. Due to the exploratory nature of this study, the computational scientist performing data analysis was not blinded to group allocations. However, all key analyses were carried out in an unsupervised fashion, meaning that assessment of group differences were computationally determined. Excluded data points and the reason for their exclusion are highlighted in the respective methods sections and figure legends. One non-MS / non-neurological control (Control 5) was excluded after clinical records revealed the presence of brain metastasis.

Data availability

Spatial transcriptomics data have been deposited at Gene Expression Omnibus (GEO), accession number GSE174647:
https://www.ncbi.nlm.nih.gov/geo/query/acc.cgi?acc=GSE174647
Please note, that a smaller subset of this data set, has been used in one of our previous studies[18], where it was employed to test the circumscribed hypothesis that a specific T cell type is present in the brains of progressive MS patients. As such, no further exploration of the data set was performed then, and all analyses and conclusions of the present study are completely independent.
Mass spectrometry proteomics data have been deposited to the ProteomeXchange Consortium via the PRIDE partner repository, accession number PXD026529:
https://www.ebi.ac.uk/pride/archive/projects/PXD026529

Published scRNA-seq data of PBMCs from MS patients and healthy individuals is available from GEO: GSE144744. SnRNA-seq data of human post mortem cortical brain tissue is available from GEO: GSE118257, the Sequence Read Archive (SRA): PRJNA544731, The database of Genotypes and Phenotypes (dbGaP): phs000424.v8.p1 and the Allen brain atlas (https://portal.brain-map.org/atlases-and-data/rnaseq/human-m1-10x; https://portal.brain-map.org/atlases-and-data/rnaseq/human-multiple-cortical-areas-smart-seq). Literature curated ligand-receptor pairings are available from https://www.cellphonedb.org/ (v 2.0). Bulk RNA-seq data of human post mortem samples from 54 tissues is available from https://www.gtexportal.org/home/ (GTEX V8).

Methods references

59. Maynard, K. R. *et al.* Transcriptome-scale spatial gene expression in the human dorsolateral prefrontal cortex. *Nat Neurosci* **24**, 425–436 (2021).

60. Chen, W.-T. *et al.* Spatial Transcriptomics and In Situ Sequencing to Study Alzheimer's Disease. *Cell* (2020) doi:10.1016/j.cell.2020.06.038.

61. Wong, K., Navarro, J. F., Bergenstråhle, L., Ståhl, P. L. & Lundeberg, J. ST Spot Detector: a web-based application for automatic spot and tissue detection for spatial Transcriptomics image datasets. *Bioinformatics* **34**, 1966–1968 (2018).

62. Jemt, A. *et al.* An automated approach to prepare tissue-derived spatially barcoded RNA-sequencing libraries. *Sci Rep-uk* **6**, 37137 (2016).

63. Hafemeister, C. & Satija, R. Normalization and variance stabilization of single-cell RNA-seq data using regularized negative binomial regression. *Genome Biol* **20**, 296 (2019).

64. Butler, A., Hoffman, P., Smibert, P., Papalexi, E. & Satija, R. Integrating single-cell transcriptomic data across different conditions, technologies, and species. *Nat Biotechnol* **36**, 411–420 (2018).

65. Love, M. I., Huber, W. & Anders, S. Moderated estimation of fold change and dispersion for RNA-seq data with DESeq2. *Genome Biol* **15**, 550 (2014).

66. Aibar, S. *et al.* SCENIC: single-cell regulatory network inference and clustering. *Nat Methods* **14**, 1083–1086 (2017).

67. Langfelder, P. & Horvath, S. WGCNA: an R package for weighted correlation network analysis. *Bmc Bioinformatics* **9**, 559 (2008).

68. Zhang, B. & Horvath, S. A General Framework for Weighted Gene Co-Expression Network Analysis. *Stat Appl Genet Mol* **4**, Article17 (2005).

69. Csárdi, G. & Nepusz, T. The igraph software package for complex network research. *InterJournal Complex Systems* **1695**, (2006).

70. Yu, G., Wang, L.-G., Han, Y. & He, Q.-Y. clusterProfiler: an R Package for Comparing Biological Themes Among Gene Clusters. *Omics J Integr Biology* **16**, 284–287 (2012).

71. Shannon, P. *et al.* Cytoscape: A Software Environment for Integrated Models of Biomolecular Interaction Networks. *Genome Res* **13**, 2498–2504 (2003).

72. Gu, Z., Gu, L., Eils, R., Schlesner, M. & Brors, B. circlize implements and enhances circular visualization in R. *Bioinformatics* **30**, 2811–2812 (2014).

73. Colic, M. *et al.* Identifying chemogenetic interactions from CRISPR screens with drugZ. *Genome Med* **11**, 52 (2019).

Extended Data Figures

Figure #	Figure title	Filename	Figure Legend
Extended Data Fig. 1	Cell type signatures	FigS1.jpg	Enrichment of intact neuronal signature and cell type marker signatures in scRNA-seq and snRNA-seq data sets[10,11,13,22,23] aggregated per sample for *n* = 47 (intact neurons), *n* = 20 (B cells), *n* = 29 (endothelial cells), *n* = 40 (microglia), *n* = 20 (monocytes), *n* = 47 (oligodendrocytes), *n* = 41 (OPC) and *n* = 20 (T cells) biological replicates. Box plots centered on median, bounds defined between the 25th and 75th percentile with minimum and maximum defined as median ± 1.5 x interquartile range and whiskers extending to the lowest / highest value within this range.
Extended Data Fig. 2	Relation of spatial transcriptomics to neuropathological assessment	FigS2.jpg	**a**, HE-staining of *n = 1* cortical brain tissue section from patient MS1 used for spatial transcriptomics. **b**, Structural annotations. **c**, Spatial transcriptomics-based mapping of intact neuronal signature enrichment values onto gray matter. **d**, Spatial transcriptomics-based mapping of microglial signature enrichment values onto gray matter. **e**, Immunohistochemistry for myelin oligodendrocyte glycoprotein (MOG) of *n* = 1 tissue section adjacent to a. **f**, Oil Red O staining of *n* = 1 tissue section adjacent to a.
Extended Data Fig. 3	GO term enrichment maps	FigS3.jpg	GO term enrichment maps for gene co-expression modules. Nodes represent GO terms; edges connect terms that share genes. Groups of similar GO terms are jointly labelled for clarity. Only significantly (FDR-adjusted p value ≤ 0.1, methods) enriched GO terms for each module are shown. GO term networks with less than three nodes are not depicted unless no other terms were enriched in a module. All individual GO terms ranked by adjusted p values are listed in Supplementary Table 3.
Extended Data Fig. 4	Exclusion of potential age and sex bias and proteomic validation of ligand–receptor analysis results	FigS4.jpg	A potential bias resulting from comparing MS patients, who were on average younger and female, with older male controls (Supplementary Table 1) could impact the results of the ligand–receptor co-expression analysis (Fig. 4,5). To test for this, genome-wide RNA-expression data from post mortem cortical brain tissue of *n* = 336 donors with known gender and age from the GTEx consortium[53] was analyzed. A linear model was fitted for each gene to assess the degree to which age and sex predicted cortical gene expression (methods). **a**, Genome-wide quantification of age-/sex-bias of gene expression in cortical brain tissue. The y-axis displays the variance explained by age and sex (R^2), with the cut-off for a significant influence of age

			and/or sex on cortical expression denoted with a dotted line (FDR-adj. *p value* ≤ 0.1, linear model, two-sided). The set of differentially co-expressed ligand/receptor genes contained less age-/sex-biased genes (13.93%) than would be expected based on the overall frequency of age-/sex-biased genes in the whole genome (19.96%). **b**, Mean cortical expression of exemplary genes. *ZFY* shows a strong sex bias, *GPR26* expression is significantly influenced by age and *GPR37L1* (the top candidate from our study, compare Fig. 7b) appears to be neither influenced by age nor sex. The linear model explained 63.5% of the variance (R^2) for *ZFY* (FDR adj. *p* value = $8.1x10^{-63}$), 32.8% for *GPR26* (FDR adj. *p* value = $1.09x10^{-21}$) and 0% for *GPR37L1* (FDR adj. *p* value = 0.56). **c**, Further exploration of the 13.93% age-/sex-biased ligand–receptor genes to test whether they follow a pattern that could be explained by age/sex imbalance between our study cohorts. The only gene found to match an expected pattern was PDGFRA. **d**, Validation of ligand–receptor analysis results at the protein level. The log2 fold change between intact MS gray matter and control areas is shown for ligand/receptor genes that were detected both at the RNA and protein level. *n* = 18 control regions (RNA), *n* = 111 intact MS gray matter regions (RNA), *n* = 8 control regions (protein), *n* = 31 intact MS gray matter regions (protein). Two-sided Pearson correlation, mean centered 95% confidence band shown in gray. The correlation between ligand/receptor gene expression was positive (r = 0.41) and significant (*p value* ≤ 0.044).
Extended Data Fig. 5	Validation of snRNA-seq based cell type deconvolution	FigS5.jpg	Spatial transcriptomics data were integrated with single cell RNA-seq data in this study through enrichment score-based deconvolution[14] implemented with DEseq2[67] and AUCell[68]. To validate the applied integration approach three additional published methods for integration between single cell RNA-seq data and spatial transcriptomics, RCTD[40], spatialDWLS[41] and SPOTlight[42], were performed and the results compared. **a**, Correlation matrix for all four integration methods and all six CNS-resident cell types. All four methods are strongly correlated with each other. **b**, Representative projection of spot deconvolution results for all four integration methods at the same tissue location as in Fig. 5c. No major differences in cell type distribution are observed. **c**, Direct correlation of all alternative integration methods with enrichment score-based deconvolution for all CNS-resident cell types. *n* = 83,256 gray matter spot transcriptomes, r and p values derived using two-sided Pearson correlation,

			p values shown are FDR-adjusted. Highly significant positive correlation is observed for enrichment score-based deconvolution in comparison to each alternative method.
Extended Data Fig. 6	Correlation between ligand–receptor co-expression and module expression	FigS6.jpg	Two-sided Pearson correlations between each model and each ligand–receptor interaction are shown.
Extended Data Fig. 7	Organ immunohistochemistry	FigS7.jpg	**a,b**, Immunohistochemistry of indicated proteins in representative tissues. Image credit: Human Protein Atlas[54]. Only stainings based on antibodies whose reliability was classified as 'supported' or 'enhanced' in the Human Protein Atlas are shown. For image URLs see Supplementary Table 6. Matching proteins for transcripts found to be **a**, CNS-enriched or **b**, not enriched in the CNS at the RNA level.

Tables

	Number	Filename	Legend
Supplementary Table	1	table1_donors_samples.xlsx	**Study cohort information.** Metadata associated with each donor (sheet 'donor characteristics') and with each sample (sheet 'sample characteristics') are provided.
Supplementary Table	2	table2_gene_signatures.xlsx	**Gene signatures.** Cell type marker gene signatures extracted from single cell / single nuclei RNA-sequencing data sets (methods) are provided for intact cortical neurons (sheet 'Intact neuronal consensus sign.) and other cell types supporting the cell type deconvolution analysis (sheet 'cell type marker signatures').
Supplementary Table	3	table3_go_terms.xlsx	**GO terms.** Unique gene ontology (GO) terms, significantly enriched (FDR-adjusted *p* value ≤ 0.1, enrichGO algorithm, methods) in gene co-expression modules.
Supplementary Table	4	table4_LR_interactions.xlsx	**Annotations of ligand-receptor interactions differentially co-expressed between intact MS gray matter and control tissue.**

			The table provides additional information for each significant (FDR-adjusted *p* value ≤ 0.1, unpaired two-sided t-tests) interaction, including a reference for experimental validation of the ligand–receptor relationship (ref_interaction_pubmed_id) and supporting literature for the classification as trophic factor, anti-inflammatory factor or pro-inflammatory factor (annotation_ref_pubmed_id). In addition, the numeric values for the mean absolute module membership (mean_abs_module_membership) and CNS-specificity score (mean_ratio_CNS_nonCNS) are listed.
Supplementary Table	5	table5_in_vivo_perturbations.xlsx	**Published *in vivo* perturbations.** The table provides additional details for the analysis presented in Fig. 6. The sheets 'Candidate genes queried' and 'Disease models queried' summarize the search terms that were combined as queries (see sheet 'Queries') for Europe PMC searches. Raw search results are listed in the sheet 'Search results'. The extracted perturbations of candidate ligand–receptor interactions (methods) are listed in the sheet 'Perturbations_identified'.
Supplementary Table	6	table6_human_protein_atlas_URLs.xlsx	**Human protein atlas URLs.** Web addresses for each image used from the human protein atlas are provided.
Supplementary Table	7	table7_oligonucleotides_ST.xlsx	**Oligonucleotide sequences.** Sequences are provided for oligonucleotides referred to in the methods section describing spatial transcriptomics.
Supplementary Table	8	table8_software.xlsx	**Software versions.** The table lists all software used for data processing, analysis and data visualization, including version, reference and web address.